High resolution variability of the ocean carbon sink

Luke Gregor[1], Jamie Shutler[2], and Nicolas Gruber[1]

[1]Environmental Physics, Institute of Biogeochemistry and Pollutant Dynamics, ETH Zurich, Zürich, Switzerland

[2]Centre for Geography and Environmental Science, University of Exeter, Penryn, Cornwall, UK

Key Points:

- Surface ocean concentration and air-sea fluxes of carbon dioxide are estimated at 8-daily, quarter degree resolution with a neural network.
- Variability at subseasonal timescales contributes substantially to the total variability of the ocean carbon sink.
- The high-resolution data provide novel observational insights into regional and ephemeral processes, such as upwelling and hurricanes.

Corresponding author: Luke Gregor, `luke.gregor@usys.ethz.ch`

Abstract

Measurements of the surface ocean fugacity of carbon dioxide (fCO_2) provide an important constraint on the global ocean carbon sink, yet the gap filling products developed so far to cope with the sparse observations are relatively coarse (1°x1° by 1 month). Here, we overcome this limitation by using the newly developed surface Ocean Carbon dioxide Neural Network (OceanCarbNN) method to estimate surface ocean fCO_2 and the associated air sea CO_2 fluxes (FCO_2) globally at a resolution of 8-daily by 0.25°x0.25° (8D) over the period 1982 through 2022. Globally, the method reconstructs fCO_2 with accuracy similar to that of low-resolution methods ($\sim$19 µatm), but improves it in the coastal ocean. Although global ocean CO_2 uptake differs little, the 8D product captures 15% more variance in FCO_2. Most of this increase comes from the better-represented subseasonal scale variability, which is largely driven by the better resolved variability of the winds, but also contributed to by the better resolved fCO_2. The high-resolution fCO_2 is also able to capture the signal of short-lived regional events such as coastal upwelling and hurricanes. For example, the 8D product reveals that fCO_2 was at least 25 µatm lower in the wake of Hurricane Maria (2017), the result of a complex interplay between the decrease in temperature, the entrainment of carbon-rich waters, and an increase in primary production. By providing new insights into the role of higher frequency variations of the ocean carbon sink and the underlying processes, the 8D product fills an important gap.

Plain Language Summary

The ocean is important for the climate, as it takes up about a quarter of the carbon dioxide (CO_2) we release into the atmosphere. To determine this carbon sink, we measure the levels of carbon dioxide in the surface of the ocean. However, these measurements are limited to where ships measure CO_2, leaving gaps in our understanding. To fill in these gaps, statistical methods are used, but previous approaches lack fine-scale detail. We overcome this limitation with a new neural network approach that estimates CO_2 with more detail, with estimates every 8 days, at 25 km, compared to previous 100 km monthly estimates. Globally, our method is as accurate as the previous methods, being slightly more accurate in coastal areas. Although the total amount of carbon the ocean absorbs globally remains consistent, our results show more variability. Our method also detects short-lived local events, such as coastal upwelling and hurricanes. For example, our results show that after Hurricane Maria in 2017, the ocean surface had lower carbon dioxide. Overall, our detailed results give us new information about the small-scale changes in the ocean carbon sink and helps us fill in a gap in our understanding of surface ocean CO_2.

1 Introduction

The global ocean is playing a pivotal role in limiting global warming by having absorbed approximately 25% of the anthropogenic carbon dioxide (CO_2) emissions over the past 250 years (Sabine et al., 2004; Gruber, Clement, et al., 2019; Müller et al., 2023; Khatiwala et al., 2013). Although this uptake fraction has remained remarkably stable over time (Friedlingstein et al., 2022), the magnitude of the ocean carbon sink has varied substantially around this trend (Landschützer et al., 2015, 2016; Gruber, Landschützer, & Lovenduski, 2019; DeVries et al., 2023; McKinley et al., 2020; Rödenbeck et al., 2022; Bennington et al., 2022). The strongest evidence supporting this variability comes from observations of the surface ocean CO_2 concentration (generally expressed in terms of its fugacity, $f\mathrm{CO}_2$), from which the air-sea CO_2 flux ($F\mathrm{CO}_2$) can be inferred (R. H. Wanninkhof, 2014; Fay et al., 2021). Since the $f\mathrm{CO}_2$ observations are sparse in time and space, gap filling techniques are required to map them to the time-and-space continuous product needed for estimating the strength of the global ocean carbon sink over time (Rödenbeck et al., 2015; Fay et al., 2021). Most commonly, statistical or machine learning techniques are used to fill this gap (Telszewski et al., 2009; Landschützer et al., 2013; Rödenbeck et al., 2015; Gregor et al., 2019; Iida et al., 2021; Chau et al., 2022; Gloege et al., 2022), although also geospatial and data assimilation-type methods are used (Rödenbeck et al., 2022; Bennington et al., 2022). Owing to their global nature and good temporal coverage, satellite observations have proven to be key enablers for all gap filling methods (Shutler et al., 2020, 2024).

Typically, these $f\mathrm{CO}_2$ gap-filled products are produced at a monthly $1^\circ\times1^\circ$ resolution (henceforth denoted by 1M). This resolution has proven to be sufficient to constrain global ocean uptake of CO_2 and its trends and variations (Landschützer et al., 2016; Gruber et al., 2023; DeVries et al., 2023; Gloege et al., 2021) as well as the seasonal variations and their changes over time (Landschützer et al., 2018; Rodgers et al., 2023). As a result, these products have played an important role in global assessments, especially those of the Global Carbon Budget (GCB) (Friedlingstein et al., 2022, 2023; Hauck et al., 2023). But there is a large amount of variability that current $f\mathrm{CO}_2$-products cannot capture, especially at the regional and subseasonal scale. Modeling studies and observations at these scales have regularly revealed $f\mathrm{CO}_2$ variations that exceed those seen in the 1M products (Yu et al., 2020; Nicholson et al., 2022; Turi et al., 2014; Arruda et al., 2015; Friederich et al., 2008; Resplandy et al., 2024). These variations are driven by finer-scale temporal features such as storms and upwelling events, but also by finer-scale spatial features, such as those associated with mesoscale circulation or strong fronts. In addition, high-frequency variations in surface winds contribute to high frequency variations in the air-sea CO_2 fluxes as well (Whitt et al., 2019).

Our current ability to constrain such high-resolution $F\mathrm{CO}_2$ and $f\mathrm{CO}_2$ variability from observations is very limited. This is, in no small part, a consequence of the segmented way the ocean CO_2 system is currently sampled (R. Wanninkhof et al., 2019). On the one hand, we have underway CO_2 measurements from ships that give a good perspective of the variability in space along a limited number of survey lines (Jones et al., 2012). On the other hand, we have time-series observations from a few sites that provide detailed temporal information (Bates et al., 2014). But we rarely have observations that cover both time and space in a synoptic manner.

The few observation-based studies clearly point to the scale of the challenge. Regarding high frequency temporal variability, a glider-based study in the Southern Ocean found that mid-latitude cyclones can induce variability up to 20 µatm within a frequency range of 1 to 10 days (Nicholson et al., 2022). Another glider-based study suggested that $p\mathrm{CO}_2$ measurements need to be taken every three days to constrain uncertainty in dynamically variable regions (Monteiro et al., 2015). Beyond the Southern Ocean, intense sporadic events like tropical cyclones and hurricanes can cause $p\mathrm{CO}_2$ fluctuations as large as 50 µatm within a two-day window (Yu et al., 2020; Bates et al., 1998; Koch et al., 2009). Mooring-based studies from various locations have also revealed variations of more than 50 µatm within days to weeks (Leinweber et al., 2009; Sutton et al., 2014, 2017; Pardo et al., 2019; Torres et al., 2021).

Regarding high resolution spatial variability, gradients exceeding several tens of µatm over tens of kilometers are regularly encountered along ship-tracks, especially in dynamic regions such as the Southern Ocean and boundary current regions. This leads to short spatial autocorrelation length scales (Jones et al., 2012). While the length scales for $F\mathrm{CO}_2$ and $f\mathrm{CO}_2$ are typically around 100 km or more in open ocean gyre regions, they decrease to less than 50 km in these dynamic regions (Murphy et al., 2001; Jones et al., 2012). These findings are corroborated by drifting buoy and saildrone-based studies in the Northeastern Atlantic and Southern Ocean, which have reported spatial gradients of $p\mathrm{CO}_2$ on the order of 10 µatm over 20 km (Boutin et al., 2008; Merlivat et al., 2009; Sutton et al., 2021).

Better resolving the fine-scale variations of the air-sea CO_2 fluxes matters for multiple reasons. First, it permits to better resolve a number of key processes that govern the ocean uptake of CO_2, providing novel insights into how the ocean carbon sink functions. Second, it permits us to assess the role of potential aliasing effects that stem from missing variability, thereby potentially aliasing our estimate of the global ocean carbon uptake (Koch et al., 2009). Third, such high-resolution products can also provide critical constraints for assessing the impact of natural or man-made perturbations, such as those associated with marine heatwaves (Mignot et al., 2022) or the purposeful release of alkaline substances to enhance the oceanic uptake of atmospheric CO_2 (González & Ilyina, 2016; Lenton et al., 2018).

First attempts to cover global finer-scale variability than 1M in gap-filled $f\mathrm{CO_2}$ products were undertaken by Rödenbeck et al. (2014) for the CarboScope Mixed-Layer Scheme (CarboScope-MLS) and by Chau et al. (2024) for the CMEMS-FFNN product. The CarboScope-MLS, while having higher temporal resolution (daily), suffers from its coarse spatial resolution of $> 2°$. CMEMS-FFNN offers superior spatial resolution, but resolves $f\mathrm{CO_2}$ only at monthly resolution. These limitations are, in part, technological in nature. For example, the commonly used Surface Ocean CO_2 Atlas (SOCAT) provides a monthly $1°\times1°$ resolution gridded product alongside the ungridded cruise tracks (Sabine et al., 2013). Similarly, remote sensing and reanalysis products are often available at monthly resolutions in addition to daily files. There are, however, a few studies that have estimated high resolution $f\mathrm{CO_2}$ (~ 5 km) at regional scales, e.g., the Gulf of Mexico (Chen et al., 2019) and South China Sea (Song et al., 2023). The regional constraint of these studies allows for simpler machine learning architecture (e.g., no clustering) that are able to predict $f\mathrm{CO_2}$ with greater fidelity than the global approaches.

In this study, we aim to bridge the "high-resolution gap" in current $f\mathrm{CO_2}$ products by generating estimates at an 8-daily, $0.25°\times0.25°$ (henceforth referred to as 8D) resolution for both $f\mathrm{CO_2}$ and $F\mathrm{CO_2}$. To achieve this, we introduce a novel machine-learning approach called the Ocean Carbon Neural Network (OceanCarbNN). OceanCarbNN builds on several lower-resolution previous approaches, but reaches an unprecedented resolution in time and space.

The paper is organized as follows: First, we outline the datasets and methodology that underlie our innovative technique. Following this, we rigorously evaluate the model's output. We then explore the implications of high-resolution $p\mathrm{CO}_2$ data on $F\mathrm{CO}_2$ variability across different temporal scales. Finally, we assess the local and global impact of these high-resolution estimates, including a case study focused on the influence of a hurricane.

2 Methods

2.1 The Ocean Carbon Neural Network method

2.1.1 Design elements of OceanCarbNN

The Ocean Carbon Neural Network (OceanCarbNN) method is a classical machine learning-based regression approach to map the sparsely observed $f\mathrm{CO}_2$ data to the global surface ocean (Rödenbeck et al., 2015). To achieve the mapping at the 8D target resolution, while maintaining robustness and scalability, several design elements are implemented, most of which build on the ideas of other studies.

The first design element concerns the target variable. We first subtract atmospheric CO_2 in order to remove most of the trend in the target variable (Ma et al., 2023). Thereafter, following Bennington et al. (2022), we remove the temperature effect from oceanic $f\mathrm{CO}_2$ leaving the non-thermal, i.e., chemically driven, part of the signal. These two transformations capture the impact of two well-understood and quantifiable drivers, such that the machine learning part is focused on the variability imparted on $f\mathrm{CO}_2$ through the other drivers, such as biology and mixing (Sarmiento & Gruber, 2006).

The second design element is that we use a prior estimate of an 8-daily climatology of $f\mathrm{CO}_2$ as a predictor. This is inspired by the works of Landschützer et al. (2015) and Denvil-Sommer et al. (2019), both of which include information on the $f\mathrm{CO}_2$ seasonal cycle, the dominant mode of variability. The first study does this through clustering based on a predefined monthly climatology of $f\mathrm{CO}_2$, and the second by removing the monthly climatological signal from $f\mathrm{CO}_2$ before training their neural network.

The third design element is that we combine decision-trees and neural-networks. For the estimation of the climatological seasonal cycle, we use Gradient Boosted Decision Trees (GBDT), thus taking advantage of the low bias nature of tree-based approaches.

For the estimation of the time-varying $f\mathrm{CO_2}$, we use a feed-forward neural network method. Theoretically, the differentiable nature of FFNNs better captures the relationships (i.e., gradients) between the $f\mathrm{CO_2}$ and its drivers (Holder & Gnanadesikan, 2021).

The fourth and final design element is that we include the rate of change of the drivers as predictors. More specifically, the difference between the current and previous time step is used for variables such as temperature and chlorophyll-a. This gradient adds additional information about the rates of change and further improves the stability of the $f\mathrm{CO_2}$ predictions between time steps.

Overall, this set of design choices improves the stability and robustness of our estimates and improves the computational efficiency (compared to other methods), which is important given that the amount of data increased by a factor of $\sim$61 by going from the typical 1M resolution to 8D.

Figure 1 summarizes the 6 steps involved in the estimation of $f\mathrm{CO_2}$ and $F\mathrm{CO_2}$ by OceanCarbNN: 1) Data preparation and preprocessing, including the detrending of the target variable by subtracting the atmospheric $\mathrm{CO_2}$ mixing ratio to form the variable $\Delta^*\mathrm{CO_2}$. 2) Machine learning part 1: Estimation of the 8-daily climatology of $\Delta^*\mathrm{CO_2}$; 3) Removal of the thermal component from $\Delta^*\mathrm{CO_2}$; 4) Machine learning part 2: Estimation of the time-variable non-thermal target $\Delta^*\mathrm{CO}_2^{nonT}$; 5) Reverse transformation of $\Delta^*\mathrm{CO}_2^{nonT}$ to obtain the time-variable $f\mathrm{CO_2}$ field; 6) Estimation of the air-sea $\mathrm{CO_2}$ fluxes, $F\mathrm{CO_2}$. The methods section, in large, describes these steps in greater detail. Furthermore, we describe the decomposition of the air-sea $\mathrm{CO_2}$ fluxes into different temporal modes of variability.

2.1.2 Step 1: Data preparation and preprocessing

The target variable is $f\mathrm{CO_2}$ from the ungridded SOCAT v2022 cruise track dataset (D. C. Bakker et al., 2016; D. C. E. Bakker et al., 2023). The data are first binned to 8-daily by 0.25°× 0.25° resolution. No weighting is applied during the binning, meaning that the data is analogous to the unweighted $f\mathrm{CO_2}$ data from the gridded SOCAT product. We then detrend the data using the $\mathrm{CO_2}$ concentration in the marine boundary layer ($x\mathrm{CO}_2^{\mathrm{mbl}}$) from Dlugokencky et al. (2021):

$$\Delta^*\mathrm{CO_2} = f\mathrm{CO}_2^{\mathrm{SOCAT}} - x\mathrm{CO}_2^{\mathrm{mbl}} \tag{1}$$

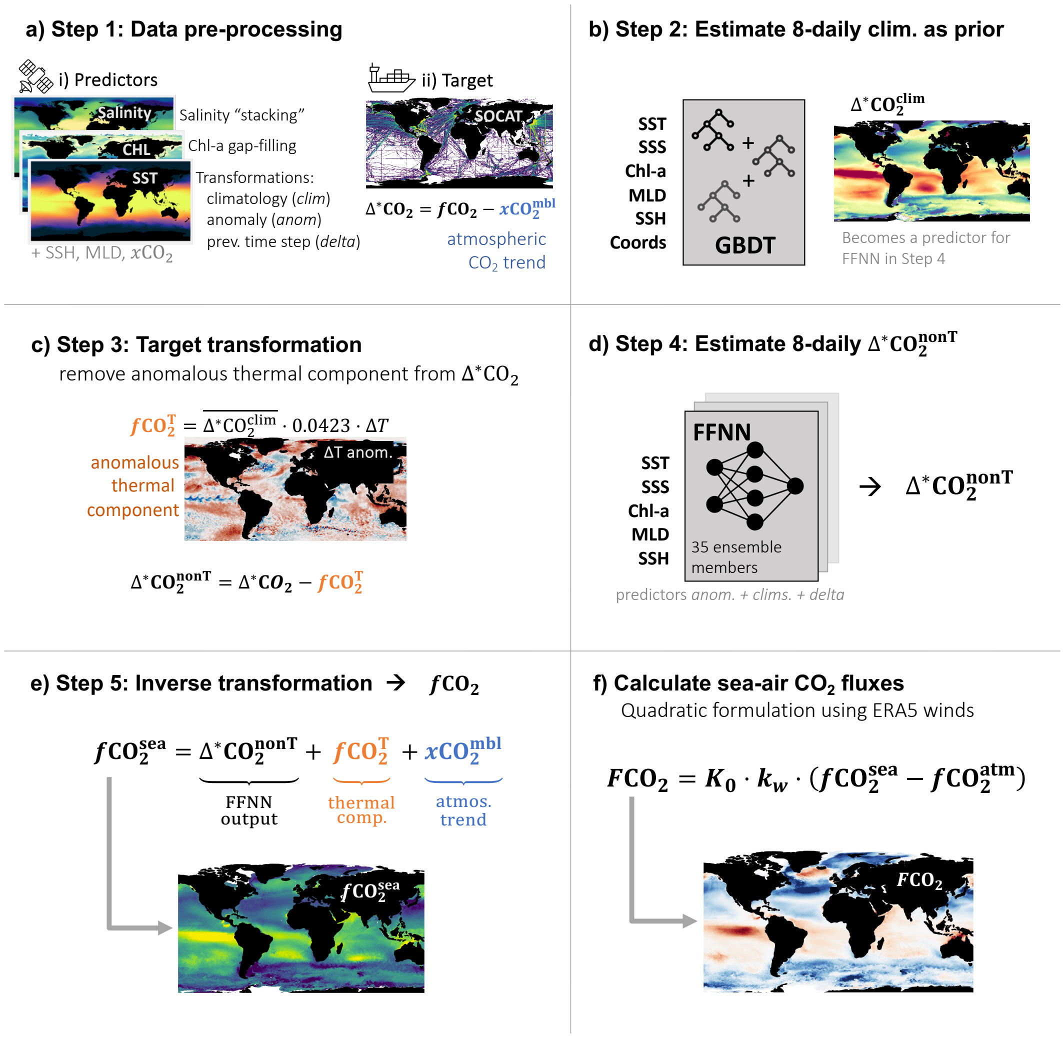

Figure 1. Diagram showing the 6 steps in the OceanCarbNN approach. (a): Step 1: Data preparation and pre-processing (Figure 2, Section 2.1.2). Notably, we remove the atmospheric CO_2 trend from SOCAT fCO_2 by removing the mole fraction of CO_2 at the marine boundary layer (xCO_2^{mbl}). This yields the variabile Δ^*CO_2. (b) Step 2: An 8-daily climatology of Δ^*CO_2 is estimated and used as a prior in step-4 (Section 2.1.3). We use Gradient Boosted Decision Trees (GBDT). (c) Step 3: The target variable is transformed by removing the anomalous thermal component, fCO_2^T (after Bennington et al., 2022) (Section 2.1.5). The resulting non-thermal component, $\Delta^*CO_2^{nonT}$, is used as the target for the next step. (d) Step 4: An ensemble of 35 FFNNs predicts $\Delta^*CO_2^{nonT}$ at 8D resolution (Section 2.1.5). (e) Step 5: Reverse transformation: The thermal component (fCO_2^T) and atmospheric trend (xCO_2^{mbl}) are added back to arrive at the OceanCarbNN estimate of fCO_2. (f) Step 6: Calculate the sea-air CO_2 fluxes with the output from the previous step (Section 2.1.7).

For the detrending, we use $x\mathrm{CO_2}$ rather than atmospheric $f\mathrm{CO_2}$ in order to avoid any unwanted impact of variations in atmospheric pressure and vapor pressure.

An important consideration for the selection of the predictor variable was the availability of these predictors at the 8D target resolution. This required some gap filling, and some merging of different data sets. The final set is summarized in Figure 2 and consists of the following predictors: atmospheric $\mathrm{CO_2}$ concentration at Mauna Loa ($x\mathrm{CO_2^{atm}}$; Tans & Keeling, 2023), sea surface temperature (SST; Merchant et al., 2019), salinity (Boutin et al., 2018; Carton et al., 2018; Droghei et al., 2016), sea surface height (SSH; Taburet et al., 2019), chlorophyll-a (CHL; Sathyendranath et al., 2023), and mixed-layer depth (MLD; Carton et al., 2018). This set of predictors is rather similar to that used by most other gap-filling methods (Rödenbeck et al., 2015), except for the use of SSH, the addition of the temporal derivatives of the drivers and prioritising the use of climate data records.

Pre-processing and transformation (Figure 1a) of these variables can be separated into: 1) gridding to 8-daily by 0.25° × 0.25°, 2) variable stacking for salinity and gap-filling for CHL, 3) separation of anomalies from climatologies (*clim, anom*), 4) calculating the difference between the current and previous time step (*delta*) which is used as a predictor. For the full description of how these data were prepared, see Supplementary Information Text S1.

2.1.3 Step 2: Estimation of 8-daily climatology

Landschützer et al. (2015) and Denvil-Sommer et al. (2019) have shown that the climatological seasonal cycle of $f\mathrm{CO_2}$ is a powerful predictor when filling the gaps. This is because to zeroth order, the seasonal cycle of $f\mathrm{CO_2}$ is relatively stationary, such that using the climatological mean value for a given month is a good first guess of that month's value. Both aforementioned studies used the climatology of Takahashi et al. (2009) and interpolated it to the 1° resolution of their product. Here, we estimate this climatology ourselves, especially since we require it at 8D resolution.

We estimate the quarter-degree 8-daily climatology of $\Delta^*\mathrm{CO_2}$ using Gradient Boosted Decision Trees. We use climatological predictors along with transformations of the time and space coordinates (Figure 2) — see Supplementary Information Text S1. The estimated $\Delta^*\mathrm{CO_2^{clim}}$ is smoothed with a rolling mean with a two-month by 0.75° window

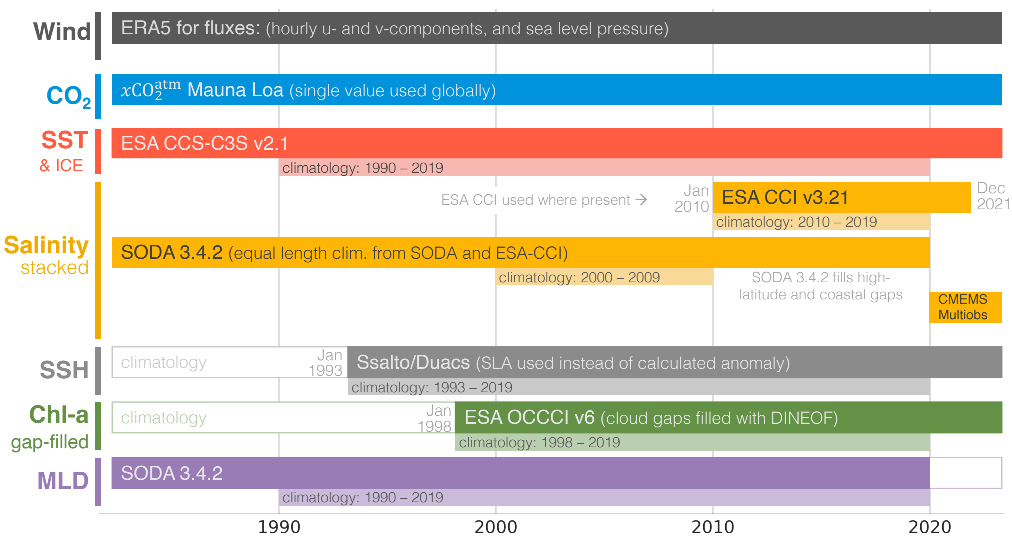

Figure 2. A Gantt chart showing the use of various datasets in the OceanCarbNN. Each variable is represented by a color, with each product having its own horizontal bar and the thinner, lighter shaded bars represent the periods over which the climatology was calculated for that variable. In the case of salinity, where products overlap in time, the high-latitude and coastal gaps of the ESA-CCI product are filled by the CMEMS-Multiobs product, with ESA-CCI always taking priority. For a full list of these products, see Table S1 in the Supplementary Information.

(seven 8-day time steps) to avoid overfitting. We choose a large temporal window, but narrow spatial window to preserve spatial gradients, particularly in the coastal regions.

2.1.4 Step 3: Target transformation

Predictor variables for the second machine learning step include all variables as anomalies, together with their 8-daily climatologies, and the differences between the current and previous time step. The target, $\Delta^*\mathrm{CO}_2^{\mathrm{nonT}}$, is estimated by removing the thermal component of $f\mathrm{CO}_2$ (Figure 1c), after Bennington et al. (2022):

$$\Delta^*\mathrm{CO}_2^{\mathrm{nonT}} = \Delta^*\mathrm{CO}_2 - (\underbrace{\overline{f\mathrm{CO}_2^{\mathrm{clim}}} \cdot 0.0423 \cdot \Delta\mathrm{T}}_{\text{thermal component}}), \tag{2}$$

where, $\overline{f\mathrm{CO}_2^{\mathrm{clim}}}$ is the long-term mean estimate of the fugacity of CO_2, and $\Delta\mathrm{T}$ is the temperature anomaly (as in Bennington et al., 2022), i.e., the anomaly relative to the long-term mean sea-surface temperature.

2.1.5 Step 4: Estimation of $\Delta^*\mathrm{CO}_2^{\mathrm{nonT}}$

We use a Feed-Forward Neural Network to estimate $\Delta^*\mathrm{CO}_2^{\mathrm{nonT}}$. This choice is based on the work of Courtois et al. (2023), who demonstrate that such networks (that are not too wide or deep) are able to extrapolate beyond the training observations. In addition, neural networks were shown to be better able to capture the true relationship between a target variable and its predictors (Holder & Gnanadesikan, 2021).

The collocated ship-track and predictor data are split into training, testing, and validation subsets. We use the same approach as Bennington et al. (2022) where every seventh month is considered a test (or validation) month. The validation subset uses the same seven-month split, but with a three-month offset. The validation split is used to avoid overfitting of the FFNN by stopping training when no improvement is observed. Test data are not used during training of the FFNN and are used to assess performance. Given the structure of our splits, seven train-test-validation splits can be created by starting on a different month in 1982 (January through July), meaning that we can fully reconstruct the SOCAT cruise tracks with only test splits (Figure S1).

We use an ensemble of FFNNs to predict $\Delta^*\mathrm{CO}_2$, with five FFNNs per train-test-validation split. Together with the 7 splits, this results in a total of 35 ensemble members. We use TensorFlow and Keras to construct our neural network ensemble (Abadi et al., 2015). Each ensemble member has two hidden layers with 64 and 32 neurons with ReLu activation (see Supplementary Information Text S2).

2.1.6 Step 5: Retransformation

The predicted output is first transformed back to Δ^*CO_2 from $\Delta^*CO_2^{nonT}$ using the thermal component of Eq. 2. The Δ^*CO_2 variable is in turn further transformed back to fCO_2 using Eq. 1. All 35 ensemble members are then averaged for the estimates of fCO_2 and the standard deviation of the ensemble is calculated (σ_{ens}).

2.1.7 Step 6: Calculation of Fluxes

We calculate sea-air CO_2 fluxes (FCO_2) using the bulk formulation:

$$FCO_2 = K_0 \cdot k_w \cdot (fCO_2 - fCO_2^{\mathrm{atm}}) \cdot (1 - ice), \tag{3}$$

where K_0 is the solubility of CO_2 in seawater from Weiss (1974), k_w the gas transfer velocity (R. H. Wanninkhof, 2014; Sarmiento & Gruber, 2006), fCO_2 is the surface ocean CO_2 fugacity predicted by OceanCarbNN, fCO_2^{atm} is the atmospheric marine boundary layer CO_2 fugacity, and *ice* is the sea-ice fraction from the temperature product shown in Figure 2. The sign convention is that a positive flux in (3) is upward, i.e., indicating outgassing of oceanic CO_2.

Atmospheric fCO_2 is calculated from the dry air mixing ratio of atmospheric CO_2 in the marine boundary layer from NOAA, i.e., xCO_2^{mbl} (Dlugokencky et al., 2021) :

$$fCO_2^{\mathrm{atm}} = xCO_2^{\mathrm{mbl}} \times (P_{\mathrm{atm}} - p\mathrm{H_2O}) \times virial\ factor, \tag{4}$$

where P_{atm} is the mean sea-level pressure from ERA5 (Hersbach et al., 2020), $p\mathrm{H_2O}$ is the partial pressure of water vapor based on Weiss and Price (1980), and the $virial\ factor$ accounts for the non-ideal behavior of CO_2 (Weiss, 1974). For k_w, we use the quadratic formulation of the sea-air CO_2 fluxes from R. H. Wanninkhof (2014) scaled for ERA5 winds:

$$k_w = 0.271 \cdot \mathrm{U}_{10}^2 \cdot \left(\frac{Sc}{660}\right)^{-1}, \tag{5}$$

where U_{10}^2 is the second moment of the wind speed, and Sc is the Schmidt number for CO_2 (Jähne et al., 1987). The second moment of the wind speed is calculated from hourly ERA5 data using u^2+v^2, where u and v are wind vectors. U_{10}^2 is then regridded in the time dimension to match the resolution of our output. The coefficient of gas transfer (0.271) was obtained by ensuring that the global mean gas transfer coefficient for the period 1990 and 2019 and for the ice-free ocean matches the constraint of $k_w = 16.5 \pm 3.2$ cm hr^{-1} (Sweeney et al., 2007; Naegler, 2009; Fay et al., 2021).

2.2 Decomposition of fluxes

We decompose the temporal variability of the air-sea CO_2 fluxes into three modes by integrating over the frequencies in the Fourier domain (after Gu et al., 2023): sub-seasonal, < 3 month frequencies; seasonal, 3 to $\sim$15 month frequencies; and interannual, > 15 month frequencies. In some cases, we further separate the interannual variability into sub-decadal (15 months to 8 years) and decadal (> 8 years) variability. To simplify the Fourier decomposition, we give all time steps the same length, i.e., $\frac{365}{46}$ days for the high-resolution 8D product and $\frac{365}{12}$ days for the 1M low-resolution product.

To identify the drivers of the air-sea CO_2 flux variability, we apply a Reynolds decomposition ($y = \overline{y} + y'$) to Eq. 3. We thereby combine k_w and K_0 as the gas transfer coefficient $k_x = K_0 \cdot k_w$, in order to focus on the role of the wind variability (Doney et al., 2009) – the temperature dependencies in k_w and K_0 account for $< 1\%$ of the variability of k_x (Woolf et al., 2016). We also look only at the role of the air-sea difference in $f\mathrm{CO}_2$, i.e., $\Delta f\mathrm{CO}_2$, since the variability of atmospheric $f\mathrm{CO}_2$ is much smaller than that of the oceanic $f\mathrm{CO}_2$. Furthermore, we neglect the role of sea-ice variations. With these simplifications we decompose the air-sea CO_2 flux, FCO_2, as follows:

$$FCO_2 = \underbrace{\overline{k_x} \cdot \overline{\Delta f\mathrm{CO}_2}}_{\text{mean state}} + \underbrace{k_x' \overline{\Delta f\mathrm{CO}_2}}_{\text{wind variability}} + \underbrace{\overline{k_x} \Delta f\mathrm{CO}_2'}_{f\mathrm{CO}_2 \text{ variability}} + \underbrace{k_x' \cdot \Delta f\mathrm{CO}_2'}_{\text{cross-term}} . \tag{6}$$

Since we are interested in the variability of FCO_2 we do not have to consider the first term where the long-term averages are taken for both variables. We calculate the variability as representations of the variance (σ^2). If we represent each of the terms in Eq. 6 as a, b, and c respectively, the total variance is represented by:

$$\begin{aligned}\sigma^2(a+b+c) = {} & \sigma^2(a) + \sigma^2(b) + \sigma^2(c) \\ & + \underbrace{2 \cdot \mathrm{cov}(a,b) + 2 \cdot \mathrm{cov}(a,c) + 2 \cdot \mathrm{cov}(b,c)}_{\text{covariances} \approx \text{residual}} .\end{aligned} \tag{7}$$

Given that we calculate the variance from the frequency domain, we calculate the covariance for the different modes of variability as the residual of the total and summed variances. The fraction contribution by each term is computed as:

$$\frac{\sigma^2(\text{wind})}{\sigma^2(\text{total})}, \frac{\sigma^2(f\text{CO}_2)}{\sigma^2(\text{total})}, \frac{\sigma^2(\text{cross term})}{\sigma^2(\text{total})}, \frac{\text{covariances}}{\sigma^2(\text{total})}. \tag{8}$$

Note that since the covariances can be negative, the fractional contribution can be negative, too.

3 Evaluation and assessment

We first evaluate the 8D $f\text{CO}_2$ product estimated by OceanCarbNN by determining the large-scale offsets against the test and training data, and by comparing these offsets against the ensemble spread that we use as an estimate of the prediction uncertainty. We then investigate in what way the high-resolution product is able to capture finer-scale structures in time and space. To this end, we focus on high-frequency observations from open ocean mooring stations (Sutton et al., 2019). We also assess how well the high-resolution estimates can track high-resolution spatial features observed along cruise tracks.

3.1 Uncertainties

To determine the bias and root mean squared differences (RMSD) of the 8D product against the SOCAT data, we rely only on predictions that have not been used to train the subset of ensemble members. Given that we use an ensemble of results where the starting month changes (1-7), we have a complete representation of the SOCAT dataset (Figure S1; Gregor et al., 2019; Bennington et al., 2022).

The unweighted bias and RMSD for the $f\text{CO}_2$ estimated by OceanCarbNN are low at a global scale at -0.06 µatm and 19.2 µatm, respectively (Table S2), where a negative bias indicates that OceanCarbNN underestimates $f\text{CO}_2$ relative to SOCAT. The open (coastal) ocean has a bias of 0.07 µatm (-0.23 µatm) and an RMSD of 13.0 µatm (25.4 µatm) (Figure 3, Table S2), where the coastal ocean is defined as the ocean region within 300 km from the coast or the 1000 m isobath (Laruelle et al., 2017). Given the spatial and seasonal inhomogeneity in the SOCAT observations, biases and RMSDs are also assessed over time and space (Figure 1 with weighted averages). We assess both metrics for three latitude bands: the high northern (blue lines; > 35°N) and southern latitudes (yellow lines; > 35°S) and the bounded lower latitudes (red).

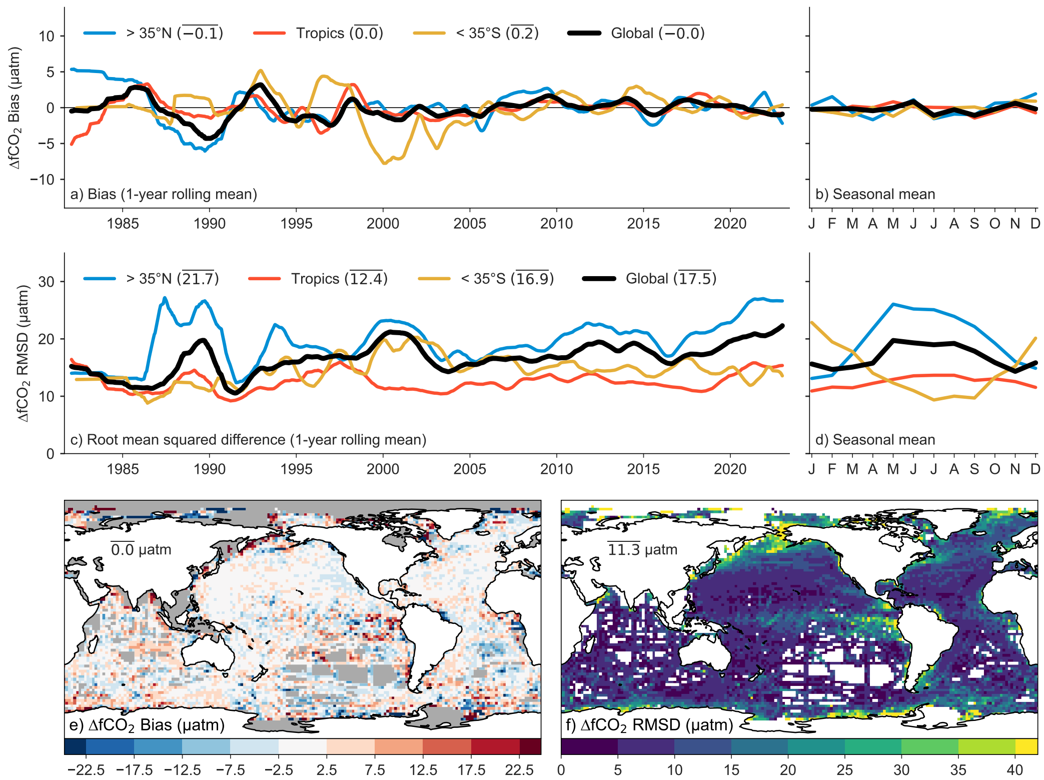

Figure 3. Metrics using test data estimates from OceanCarbNN. Time series on the left show latitudinally averaged biases (a) and root mean squared difference (RMSD in c) with a one-year rolling mean applied. The legend also contains the time-averaged mean values (in µatm) weighted by number of samples. The smaller time series figures on the right show seasonally averaged biases (b) and RMSD (d). The maps below show test bias (e) and RMSD (f) with the values showing the spatial average of the respective metrics weighted by area.

Biases are larger and more variable before 2000 when data are more sparse (Figure 3a). The spatial separation also reveals that biases compensate meridionally, resulting in lower global biases due to aggregation. There is no seasonality in the biases in any of the latitude bands. Spatially (Figure 3e), biases are mostly low ($|bias| < 2.5$ µatm) except for the coastal regions and a few open ocean regions, e.g., the southern Indian Ocean, where there is a positive bias (red in Figure 3e).

In the northern high latitudes, the RMSD increases slightly over time ($\sim$15 to >20 µatm; blue line in Figure 3c). This is likely due to the increase in the variance of the training data over time, particularly in the coastal ocean, where there is typically higher biogeochemical complexity (Figure S2). The RMSD for the tropics and southern regions remains constant ($\sim$15 µatm) throughout the forty-year period, with no significant slope. On average, RMSDs are larger in the summer months compared to the winter months ($\sim$25 µatm vs. $\sim$15 µatm) of both the northern and southern high latitudes (blue and yellow lines in Figure 3d). The seasonality of the RMSD in the low-latitudes (red line in Figure 3d) is lower by comparison, but has a slight bias to the Northern Hemisphere summer, likely due to the Northern Hemisphere sampling bias.

At a global scale, the spatial distribution of the RMSD resembles the ensemble standard deviation (σ_{ens}) with a spatial correlation r^2 of 0.65 for the time averaged maps. This suggests that the ensemble spread is a good indicator of the spatial structure of the quality of the estimated $f\text{CO}_2$. This relationship was exploited by Chau et al. (2024) who scaled σ_{ens} to match the RMSD as closely as possible. Here, we follow the same idea to obtain a global map of uncertainty of our 8D product, but we simply multiply σ_{ens} with a factor of 5.7, i.e., the global mean ratio of $\frac{\overline{\text{RMSD}}}{\overline{\sigma_{\text{ens}}}} = \frac{11.3}{2.0}$.

3.2 Assessing spatial and temporal scales of variability

The benefit of estimating $f\text{CO}_2$ at high resolution becomes most obvious when comparing the estimated product against the raw observations in SOCAT. The majority of the SOCAT data set consists of ship cruise tracks. In Figure 5, we compare three representative cruise tracks in the Atlantic and Pacific with the OceanCarbNN test-subset of $f\text{CO}_2$, where the test-subset is a subset of our output that has not been trained with the data that it is estimating. Along all three tracks, the large-scale variability of the SOCAT $f\text{CO}_2$ observations is well represented. In open ocean regions, the RMSD scores

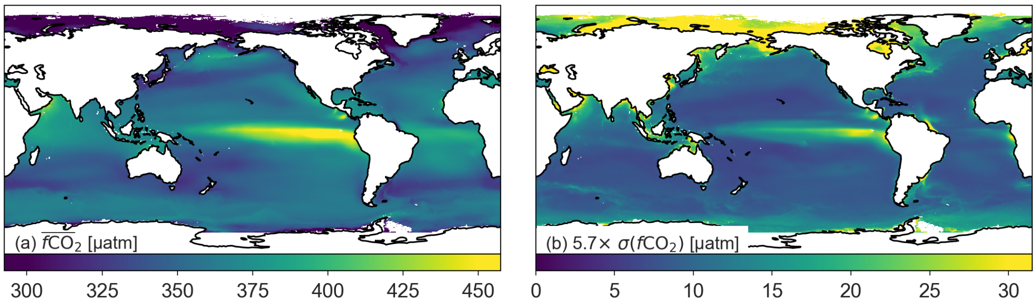

Figure 4. (a) The long-term mean of $f\mathrm{CO}_2$ for 1982 to 2022 and (b) the scaled standard deviation (5.7σ) of the ensemble members of OceanCarbNN.

are actually substantially lower than the global average. An exception to this occurs in poorly sampled regions, such as the South Atlantic gyre (Figure 5d, where the regional biases can be $> |5|$ µatm). Most important, however, is the fact that the high-resolution product captures a substantial fraction of the fine-scale structures of the observed $f\mathrm{CO}_2$. For example, the 8D product properly represents the strong outgassing signals associated with the upwelling driven by the gap winds off the coast of Central America (Figure 5a). The impact of these ephemeral winds, called Tehuano and Papagayo jets, on the surface ocean CO_2 system on ocean biogeochemistry has been well documented by in situ measurements (Chapa-Balcorta et al., 2015), but is generally not well captured by the global 1M products. Further, the 8D product properly captures the magnitude of the equatorial upwelling in both the Atlantic and Pacific (Figure 5c,d), as well as the strong variations off the coast of Europe (Figure 5d). At the same time, some deficiencies also emerge. The specific structure of the upwelling signal associated with the gap winds is missed, as is the exact location of the equatorial upwellings offset. Furthermore, the signals of two tropical instability waves in the equatorial Pacific (Figure 5c) are completely missed by the 8D product. Finally, the neural network cannot capture some extremely sharp gradients observed near New Zealand (Figure 5c).

Similar successes and limitations of the 8D product can be identified when comparing it with high-frequency observations from long-term moorings. Within SOCAT, we identified five open-ocean mooring programs that have measured $f\mathrm{CO}_2$ at sub-daily frequency for multiple years (Sutton et al., 2019; D. C. Bakker et al., 2016). These are located in the Pacific and the Pacific sector of the Southern Ocean (Figure 6). The observed $f\mathrm{CO}_2$ is well represented by the $f\mathrm{CO}_2$ estimated by OceanCarbNN at locations

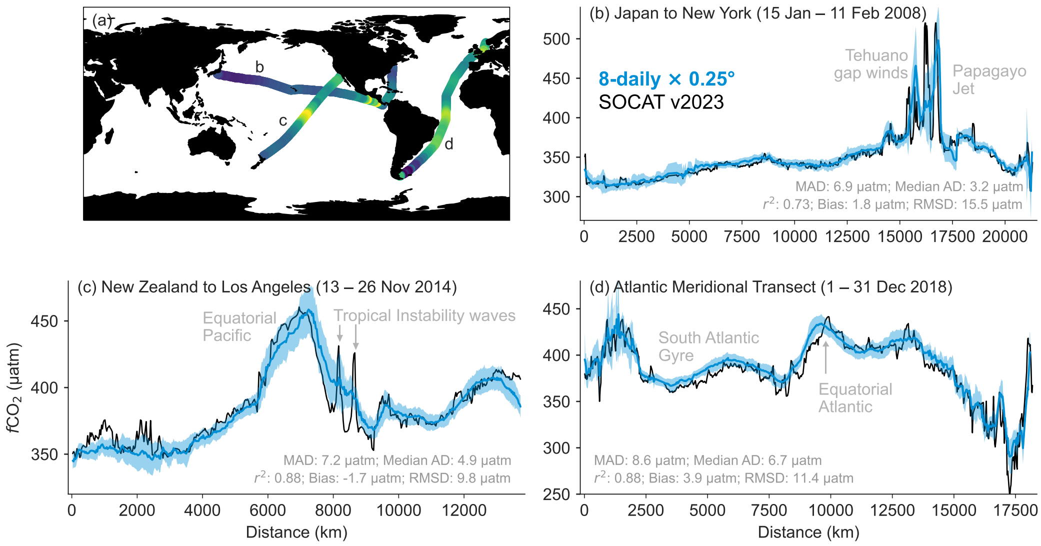

Figure 5. Comparison of the observed fCO_2 along three selected cruise tracks contained within the SOCAT database (black lines) with the estimated fCO_2 from the 8D OceanCarbNN test-subset (blue lines). The blue envelope shows the scaled ensemble standard deviation ($5.7\sigma_{\mathrm{ens}}$). (a) Locations of the cruise tracks with the colors indicating the measured fCO_2. (b) Transect from Japan to New York occupied between Jan 15, 2008 and Feb 11, 2008. (c) Transect from New Zealand to Los Angeles occupied between Nov 13, 2014 and Nov 26, 2014. (d) Transect between Southampton and Punta Arenas occupied between Dec 1, 2018 and Dec 31, 2018 as part of the Atlantic Meridional Transect program. The distance along the x-axes of the cruise tracks (b, c, d) is plotted with zero being the most western point, regardless of the actual direction of travel.

with a large seasonal cycle. The 8D product captures 90% of the variability observed at the KEO mooring off the coast of Japan (Figure 6a), 82% at the SOFS mooring south of Tasmania (Figure 6e) and 71% at the STRATUS mooring site off the coast of South America (Figure 6f). Also, shorter-term variations are generally well captured at these three sites. The performance of the OceanCarbNN 8D product is somewhat weaker at the other two sites. While the $f\mathrm{CO}_2$ estimates at the PAPA mooring location (Figure 6b) are able to represent most of the seasonal variability, some extremes are not captured. This leads to only 50% of the observed variability being captured by the OceanCarbNN 8D product. In the equatorial Pacific (TAO125W in Figure 6d) the OceanCarbNN 8D product appears to miss a substantial fraction of the high-frequency variability. Much of this variability is caused by equatorial instability waves. This mismatch is consistent with the mismatches seen in the Equatorial Pacific when analyzing the cruise line data (Figure 5c).

In summary, the 8D product is able to resolve simultaneously large and fine-scale structures in the observed $f\mathrm{CO}_2$, with a few important exceptions. One example are very short-lived excursions, such as those associated with tropical instability waves. This is largely a consequence of these features having a propagation speed of around 30 km day^{-1} (Legeckis, 1977), such that an 8-day resolution ∼25 km product is insufficient to correctly capture their dynamics.

4 Patterns and variability of $f\mathrm{CO}_2$

4.1 Representation of high-resolution features

Recognizing some shortcomings of our high-resolution mapped $f\mathrm{CO}_2$ product, it is nevertheless instructive to visualize its strengths in representing fine-scale features previously not seen in gap filled $f\mathrm{CO}_2$ products. In Figure 7 we depict 5 snapshots from different regions of the global ocean (Supplementary Information Video S1). The 8D estimates are able to represent a lot of fine-scale spatial variability in $f\mathrm{CO}_2$ that hitherto could not be seen in the 1M products. For example, the 8D estimates depict important $f\mathrm{CO}_2$ details in the eastern boundary upwelling regions off northwestern Africa (Figure 7a) and off the U.S. West Coast (Figure 7b). Of special note are the high $f\mathrm{CO}_2$ values tagging the coasts, reflecting recently upwelled waters, and the rapid offshore decrease of $f\mathrm{CO}_2$ owing primarily to strong biological drawdown. Also, the filamentous features

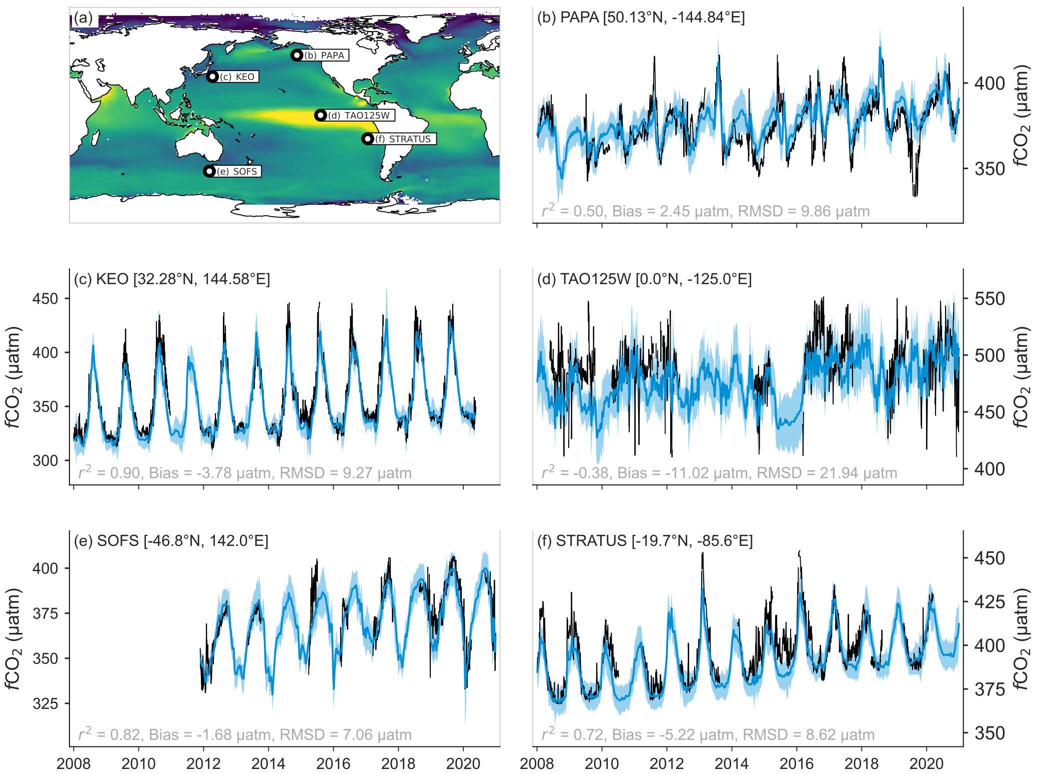

Figure 6. Mooring stations from Sutton et al. (2019) where fCO_2 was measured. Blue lines show the OceanCarbNN test-subset of ΔfCO_2, with the blue envelope showing the scaled ensemble standard deviation ($5.7\sigma_{\text{ens}}$). Black lines show the measured mooring data resampled to a daily resolution. Model metrics are shown in gray in the bottom of each plot. Note that these estimates are not used to train the model. The map (c) shows the location of the moorings. Mooring locations roughly match the subplot locations.

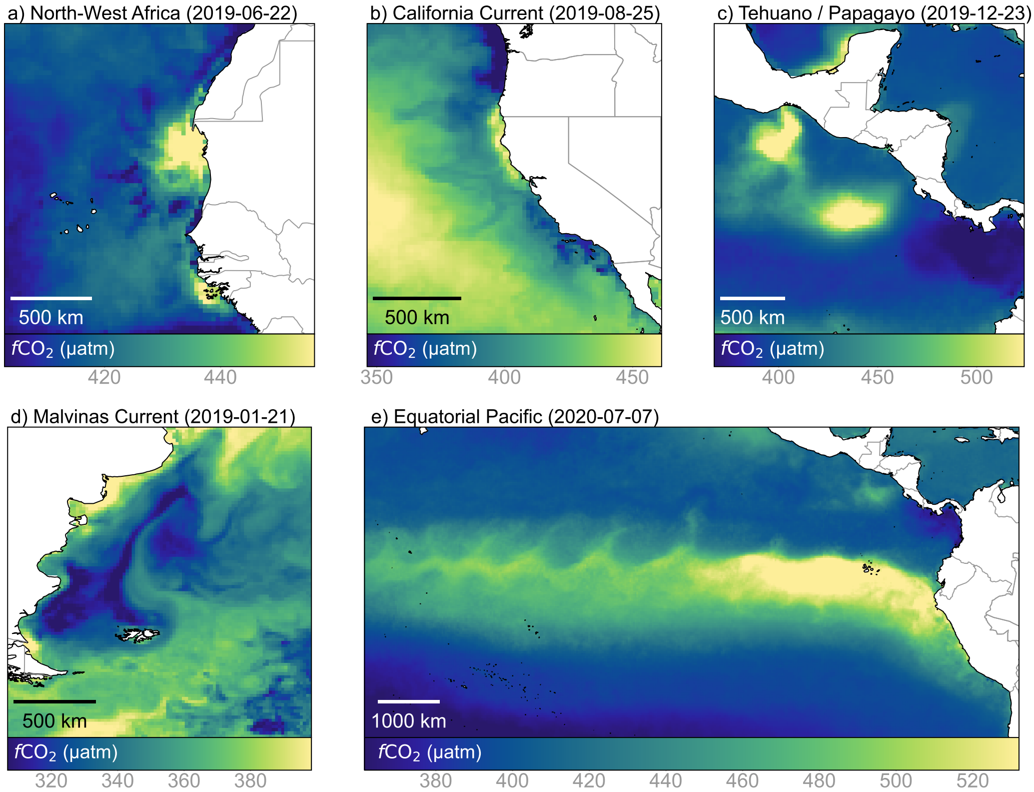

Figure 7. fCO_2 for different regions with the period represented shown by the date in brackets. (a) North-West African coastline, (b) The North-West coastline of the USA where the cal, (c) the West coast of Central America where the Tehuano gap winds, and Papagayo Jet winds occur, (d) the Malvinas (Falkland) current off the southeast coast of Argentina, (e) the equatorial Pacific from 165°W to 75°W.

of these low fCO_2 waters are clearly visible. These structures correspond very well to detailed regional observations and modeling studies (Turi et al., 2014; Lachkar & Gruber, 2013; Friederich et al., 2002).

Similarly, off the West coast of Central America, the 8D estimates reveal the spatial extent of the upwelling driven maxima in fCO_2 downstream of the Papagayo and Tehuantepec gaps (Figure 7c). Despite the ephemeral nature of these gap winds, which last for hours to several days (Romero-Centeno et al., 2003; Liang et al., 2009), their oceanic signatures remain for long enough to be picked up well by our 8 daily product. The spatial structure of these mountain gap wind features in fCO_2 are consistent with what is known from in-situ observations (see comparison to the cruise data above (Figure 5a) and the work by e.g., Chapa-Balcorta et al. (2015). Still, the spatial mismatches we identified in comparison with the cruise line data suggest that the 8-daily resolution is not entirely sufficient to fully capture these ephemeral events.

The high spatial resolution is also able to resolve the very dynamic structure of the $f\mathrm{CO}_2$ in the Malvinas Current region (Figure 7d). In this region, strong biological productivity over the Patagonian shelf interacts in a complex manner with the mixing of very different waters masses, i.e., the mixing of the warm southward-flowing Brazil Current (BC) and the cold northward flowing Malvinas Current (MC) (Arruda et al., 2015). The meandering features have been seen in modeling studies (Arruda et al., 2015) and the strong gradients created by the mixing are also regularly captured in the raw SOCAT cruise data (see also Figure 5d).

And finally, in the equatorial Pacific, the 8D $f\mathrm{CO}_2$ product begins to resolve the tropical instability waves (Figure 7e). Their shapes are, however, a little distorted and overly smoothed, which is as expected given their rapid propagation speeds (Legeckis, 1977). This mismatch has already been seen in the cruise line data (see also Figure 5c) and also the mooring data from the TAO125W site (Figure 6d).

4.2 Comparison with other $f\mathrm{CO}_2$ products

The improvement of the OceanCarbNN 8D $f\mathrm{CO}_2$ estimates is also evident when comparing it to several other $f\mathrm{CO}_2$-products (Figure 8), namely, CMEMS-LSCE (1M by 0.25° Chau et al., 2024), ULB-MPI-SOMFFN (1M by 0.25° Roobaert et al., 2023), Jena-CarboScope by (daily by 2.0° Rödenbeck et al., 2014), MPI-SOMFFN by (1M by 1° Landschützer et al., 2016), and LDEO-HPD by (1M by 1° Bennington et al., 2022). Apparent in the comparison is that the fine-scale gradients of the 8-daily OceanCarbNN estimates are sharper compared to the other approaches. In this scenario, we find that the mean gradients ($\overline{\|\nabla f\mathrm{CO}_2\|}$) of OceanCarbNN $f\mathrm{CO}_2$ are 60% stronger than the two other high-resolution products (Figure 8b,c), and more than three times those of the monthly by 1° resolution products (Figure 8e,f). The gradient increases to 0.41 µatm km^{-1} when considering the 95th percentile (representing dynamic regions) or ∼8 µatm over 20 km, thus approaching the sharp gradients recorded in observational studies (i.e., ∼10 µatm over 20 km Sutton et al., 2021).

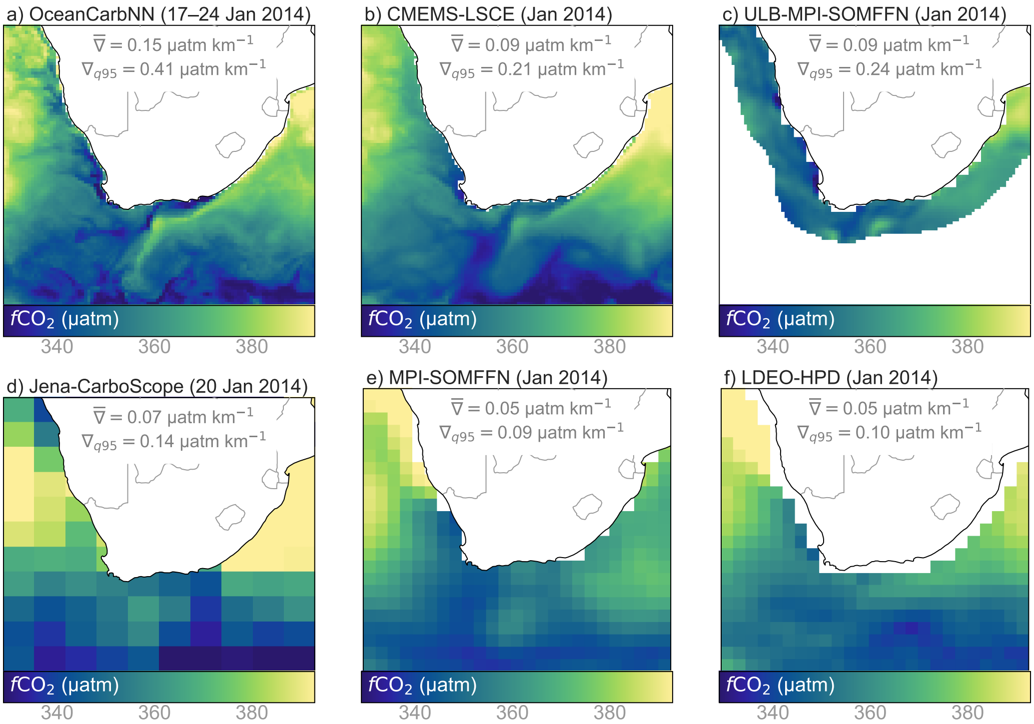

Figure 8. A comparison of fCO_2 from different fCO_2-products around Southern Africa, which includes the Agulhas Current and Benguela upwelling system. (a) OceanCarbNN fCO_2 (this study) for the 8-day period 17 to 24 January 2014 (8-daily by 0.25°). (b) CMEMS-LSCE (monthly by 0.25°) by Chau et al. (2024), (c) ULB-MPI-SOMFFN (monthly by 0.25°, coastal only) by Roobaert et al. (2023), (d) Jena-CarboScope (daily by 2°) by Rödenbeck et al. (2022), (e) MPI-SOMFFN (monthly by 1°) by Landschützer et al. (2016), and (e) LDEO-HPD (monthly by 1°) by Bennington et al. (2022). The metric $\overline{\nabla}$ represents the average horizontal gradient of fCO_2 for the plotted region and ∇_{q95} represents its 95^{th} percentile.

In summary, the OceanCarbNN method captures fine-scale spatial variability of fCO_2 with some skill. Though, there are still some high-frequency features (e.g., tropical instability waves) that are not well captured, even at the 8D resolution. However, our method is able to capture realistic variability that other methods tend to underestimate.

5 Variability of the ocean carbon sink

5.1 Mean, trend, and variability of FCO_2

The globally integrated flux FCO_2 inferred from the OceanCarbNN-8D product increases from 1.51 PgC yr^{-1} in 1990 to around -2.31 PgC yr^{-1} in 2019, corresponding to a mean trend of -0.26 PgC yr^{-1} decade^{-1} over these 3 decades (Figure 9a). Over this period (1990–2019) this gives a mean global uptake of -1.89 PgC yr^{-1}. The trend and mean uptake compares very favorably with previous estimates based on of gap filled fCO_2 products (DeVries et al., 2023). Concretely, it falls within the 1σ-bounds of the SeaFlux ensemble of 6 fCO_2 products of -1.92 ± 0.20 PgC yr^{-1} calculated with ERA5 winds (Table 4 in Fay et al., 2021). Accounting for the outgassing of natural carbon associated with the balance between river input and burial, i.e., the so-called steady-state river outgassing flux of about 0.65 PgC yr^{-1} (Regnier et al., 2022), the OceanCarbNN-8D product gives a total sink for anthropogenic CO_2 of -2.31 PgC yr^{-1} for 1990-1999, of -2.50 PgC yr^{-1} for 2000-2009, and of -2.82 PgC yr^{-1} for 2010-2019, consistent with the current best estimates of the magnitude and change of the ocean carbon sink (Gruber et al., 2023; DeVries et al., 2023).

The globally integrated flux varies substantially around these mean uptakes, with the seasonal cycle contributing the most variance (Figure 9a). There is also clear evidence of an increase in the magnitude of the seasonal cycle over time, confirming previous findings based on theory, models, and observations (Landschützer et al., 2018; Rodgers et al., 2023). In addition, clear subseasonal variations are visible in the global timeseries, as well as interannual to decadal variations. Regarding the magnitude of the interannual to decadal variability, the OceanCarbNN-8D-based flux estimates tend to be on the lower end of the spectrum compared to other gap filled fCO_2 products (DeVries et al., 2023). Still, it shows a clear stalling of the trend toward stronger uptake in the 1990s, and an

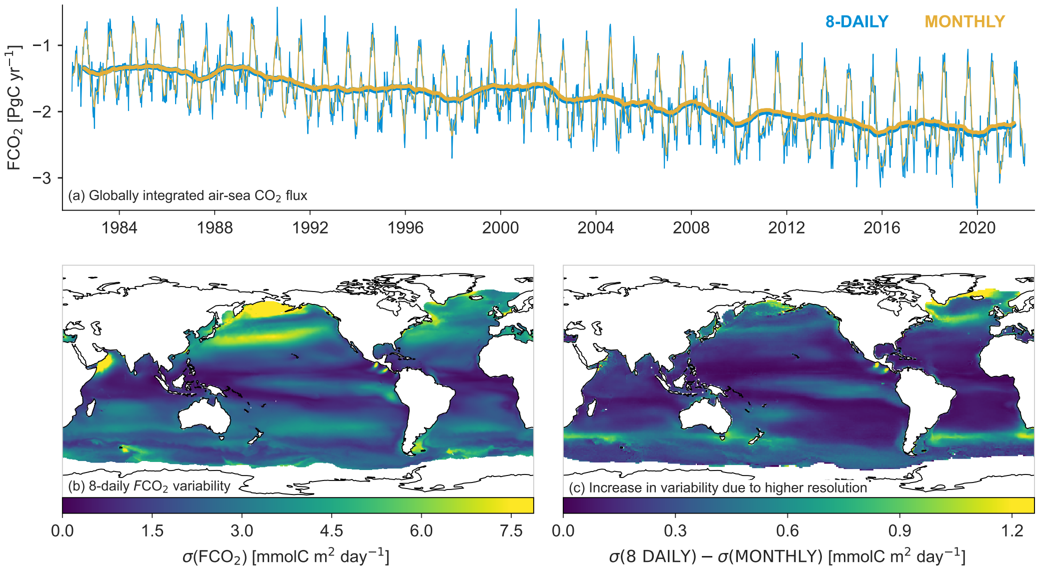

Figure 9. (a) Globally integrated sea-air CO_2 fluxes (FCO_2) for 8-daily (8D, blue) and monthly (1M, yellow) estimates, where the latter is calculated by resampling the inputs of Eq. 3 to a lower monthly $\times$ 1.0° resolution and then calculating FCO_2. (b) The standard deviation (σ) of FCO_2 for the 8D estimates. (c) The difference between (b) and the 1M (monthly $\times$ 1.0° resolution).

acceleration thereafter (Landschützer et al., 2015; DeVries et al., 2019; Gruber, Clement, et al., 2019; Gruber et al., 2023).

To assess the impact of the higher resolution on our estimates of the variability of the ocean carbon sink, we contrast our 8D estimate with a monthly by 1° $\times$ 1° (1M) estimate we obtain by averaging fCO_2 from OceanCarbNN and all other inputs to Eq. 3 to 1M (Figure 9a). Even though the 1M results are based on the averages of the 8D estimates, the global fluxes of the two products are not identical on longer timescales, i.e., the 1M product has a marginally smaller mean (1990-2019) uptake of -1.87 PgC yr^{-1}. This small difference is likely due to small co-variances between wind and ΔfCO_2, whose magnitude is scale-dependent (see below). As expected, much larger differences occur on subseasonal timescales, where the 8D product reveals higher crests and deeper troughs than the 1M product. This results in higher temporal variance, which is best analyzed spatially.

The map of the total standard deviation of the air-sea CO_2 flux FCO_2 reveals strong spatial differences ranging from near zero to more than 7 mmol C $m^{-}2$ day^{-1} (Figure 9b). The northern mid- to high-latitudes have the largest variability ($>$ 5 mmolC $m^{-}2$ day^{-1}), particularly in the Pacific basin. Some island and coastal regions (e.g., Kerguélen Plateau and Oman upwelling regions) have similarly large variability. The low-latitude regions have low variability ($<$ 1 mmolC $m^{-}2$ day^{-1}), except for the central and eastern tropical Pacific. In the global mean, the temporal standard deviation of the 8D product amounts to $\overline{\sigma}$ =2.45 mmolC $m^{-}2$ day^{-1}. This is about 10% more than the global mean temporal standard deviation $\overline{\sigma}$ of the 1M product (2.20 mmolC $m^{-}2$ day^{-1}).

While the global increase in the captured variability of the 8D product is modest, regionally, the gain in variability of the air-sea CO_2 fluxes can be much more pronounced (Figure 9c). The increase in variability is most notable along a band ($\sim$40°S) in the Sub-Antarctic Zone (SAZ) in the Southern Ocean, where the 8D product increases the variability relative to the 1M product by more than 50% in some parts. This corresponds well with the results from (Monteiro et al., 2015). The northern high-latitude Atlantic Ocean exhibits a particularly large increase in variability ($\gtrsim$ 1.5 mmolC $m^{-}2$ day^{-1}). However, the relative increase is smaller when compared with the SAZ ($<$ 40%).

5.2 Temporal decomposition of variability of $\boldsymbol{FCO_2}$

As seen already in the global timeseries, the total variability of FCO_2 is dominated by the seasonal mode (10b), i.e., by variability at timescales between 3 and 15 months. The standard deviation of the flux on this timescale goes up to more than 6 mmolC m^{-2} day^{-1}, with highest values found in the North Pacific. In contrast, the tropical regions exhibit nearly no variability on seasonal timescales. Globally, the standard deviation on seasonal timescales amounts to σ = 2.61 mmolC m^{-2} day^{-1}. The difference between σ(1M) and σ(8D) is small (0.03 mmolC m^{-2} day^{-1}), indicating that, at the seasonal scale, monthly data captures most of the variability.

The subseasonal mode ($<$ 3 months) is the next largest contributor to FCO_2 variability (σ = 1.24 mmolC m^{-2} day^{-1}, Figure 10a). The contribution to variability on these shorter timescales is dominated by the mid-latitudes and the equatorial Pacific, with some regions exceeding 2.5 mmolC m^{-2} day^{-1}. To first order, the spatial distribution of the subseasonal variability is similar to that of the seasonal variability (Pearson $R =\sim 0.69$).

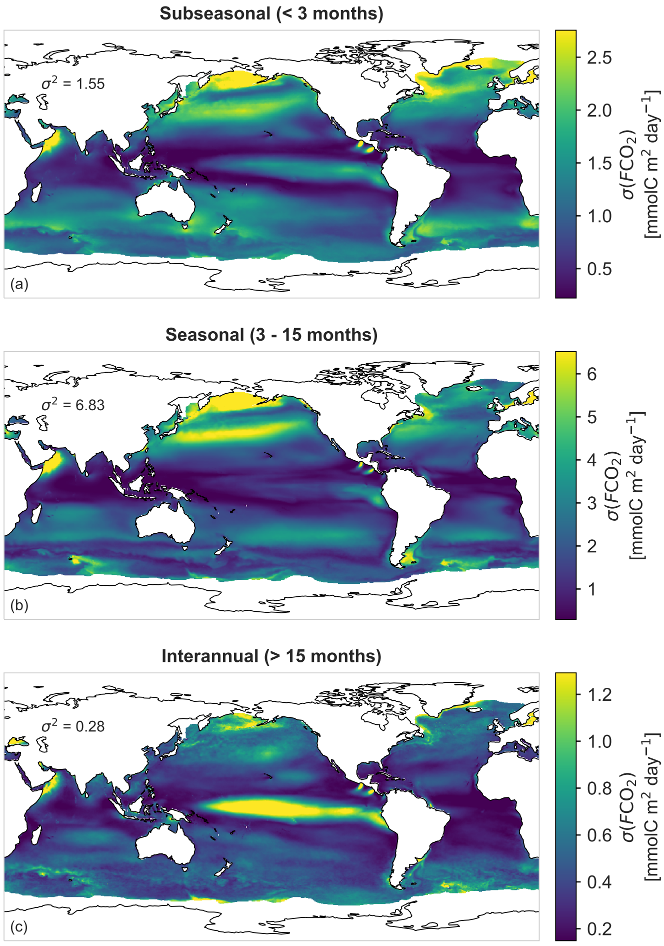

Figure 10. Maps of the standard deviation of the seasonal (a), sub-seasonal (b), and interannual (c) components of 8-daily by 0.25° FCO_2. Values on the plots show the area weighted mean of the variance in (mmolC m^{-2} day^{-1})^2. See Tables S3, S4, and S5 for low and high-resolution variance, standard deviation, and percentages, respectively.

An important difference is the strong sub-seasonal contribution in the Oman upwelling system and in the Coral Sea and Tasman Sea regions east of Australia. As expected, the gain in information by going from 1M to 8D is the largest in this sub-seasonal mode. Globally, the standard deviation increases from the 1M product nearly by a factor of 3 (see Tables S3 and S4).

Finally, variability on time-scales longer than 15 months (interannual mode) contributes the least to the overall standard deviation (Figure 10c). The global mean temporal standard deviation amounts to 0.52 mmolC m^{-2} day^{-1}, for both the 8D and 1M products. Here, the interannual variability of the equatorial Pacific driven by El-Niño—Southern

Oscillation (ENSO) is the most dominant feature, but also the higher latitudes contribute substantially, with several regions having standard deviations of more than 0.8 mmolC m^{-2} day^{-1}.

This attribution of the total variability of the air-sea CO_2 fluxes to three different modes of variability is qualitatively similar to that undertaken by (Gu et al., 2023). Perhaps unsurprisingly, there is good agreement between our studies with regard to the partitioning into subseasonal, seasonal, and interannual modes of variability. They found that the total energy of seasonal variance was an order of magnitude larger than for the subseasonal and interannual modes. This aligns with our findings, where we find an even stronger relative contribution of the subseasonal mode to the total variance, particularly at the 1M resolution.

5.3 Drivers of the variability of FCO_2

The Reynolds decomposition of the air-sea CO_2 fluxes (Eq. 6) permits us to identify the main drivers for each mode of variability (Figure 11). The seasonal variability is dominated by changes in ΔfCO_2, contributing 97% to the total seasonal changes. This is also the case for the longer modes of variability, with ΔfCO_2 contributing ∼60% to either the sub-decadal and decadal of modes variability. Wind variability, expressed in the variations in the gas transfer coefficient, matters as well, especially for the sub-decadal modes, where it contributes more than 40%. The cross-term contributions tend to be relatively unimportant for the seasonal and longer modes, contributing less than 10% to the overall variability. The co-variances between the different Reynolds terms (see Eq. 7) are negative, thus contributing negatively to the overall variability. This is likely a result of negative correlations between the mean state and the variability, e.g., high wind speed regions/times tend to be regions/times with low variations in the air-sea difference in fCO_2. This offsetting effect is particularly strong on the seasonal timescale, where it offsets the variability by more than 20%. Given the small difference between the 8D and 1M products on the seasonal and longer timescales, the results of the Reynolds decomposition are also nearly the same for these timescales.

This is not the case for the sub-seasonal mode of variability (Figure 11). And more interestingly, the large increase in the subseasonal mode of variability between 1M and 8D is due to all components of the Reynold's decomposition (Table S3). Still, the largest

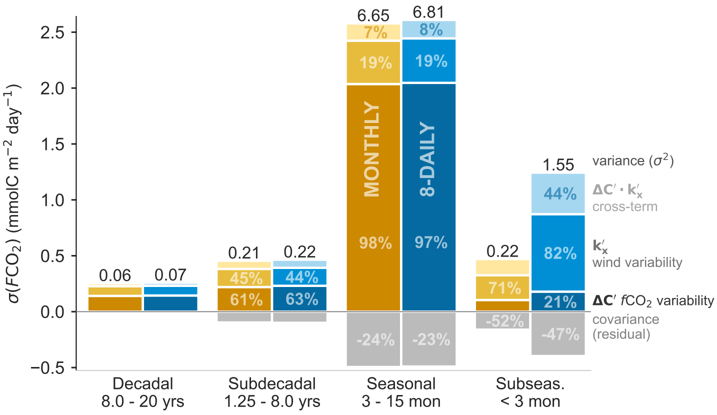

Figure 11. The contribution of $\Delta f\mathrm{CO}_2'$ (dark shading), wind and temperature (k_x', medium shading), and the cross-term ($\Delta f\mathrm{CO}_2' \cdot k_x'$, light shading) to each temporal mode of variability for 8-daily (blue) and monthly (yellow) $F\mathrm{CO}_2$. The covariances are shown in light gray. The height of the bars (positive only) shows the total standard deviation (σ) and the black numbers above each bar show the total variance (σ^2). The total height of the bar (positive and negative) represents the sum of the variances without the covariance term. The percentage contributions of k_x', $\Delta f\mathrm{CO}_2'$, cross-term, and covariances are with respect to the total variance. Thus, multiplying σ^2 with the percentage is approximately the variance for that component (within the uncertainty of rounding). See Tables S3, S4, and S5 for low and high-resolution variance, standard deviation, and percentages, respectively.

gain comes from the enhanced resolution of the wind variability as expressed in the contribution of k'_x, which increases nearly threefold from 0.40 mmolC m^{-2} day^{-1} to 1.12 mmolC m^{-2} day^{-1} (1M to 8D). The cross-term variability at the subseasonal mode also increases significantly from 0.32 mmolC m^{-2} day^{-1} to 0.82 mmolC m^{-2} day^{-1}. This indicates that there is an increase in the interaction between k_x and $f\text{CO}_2$ in the high-resolution fluxes. Mechanistically this makes sense, since wind-driven upwelling (captured by k_x) can lead to rapid changes in $\Delta f\text{CO}_2$, thus resulting in larger $F\text{CO}_2$. This is also expressed in the larger covariance term that increases by a similar magnitude (negatively) to the cross-term 11. The increase in $\sigma(F\text{CO}_2)$ due to high-resolution $\Delta f\text{CO}_2$ is 0.48 mmolC m^{-2} day^{-1} — smaller than the other subseasonal increases from 1M to 8D, but still larger than for any other mode (Table S3). Particularly striking too is the very strong negative contribution of the co-variance term, which reduces the overall variability by around 50%.

The results of the Reynold decomposition for the seasonal and longer timescales are similar to those of Gu et al. (2023). The main consistency is that, on seasonal timescales, variations in k_x, i.e., wind dominate, while at longer timescales, the $\Delta f\text{CO}_2$ term dominates. More specifically, Gu et al. (2023) attributed 66% of subseasonal variability ($<$ 3 months) to the wind component, while we attribute 71% at the 1M-scale (comparable to their study).

In summary, improved representation of sub-seasonal variability requires high-frequency information on both wind and $\Delta f\text{CO}_2$, and perhaps even more importantly, excellent information about their co-variances.

6 Case study: Hurricane Maria

The importance of co-analyzing wind variations with changes in surface ocean biogeochemistry and hence surface ocean $f\text{CO}_2$ is best shown through an example, for which we use Hurricane Maria as a case study. Hurricane Maria occurred in September 2017 and belongs to the 10 most intense Atlantic hurricanes ever recorded. It made history as it made first landfall in Puerto Rico before it turned northward and plowed through the northwestern North Atlantic. Hurricane Maria was most intense from the 17^{th} to 27^{th} of September, maintaining hurricane status throughout this period (shown by the black contours in Figure 12a-c). Thereafter, the system moved eastward. Here, we investigate

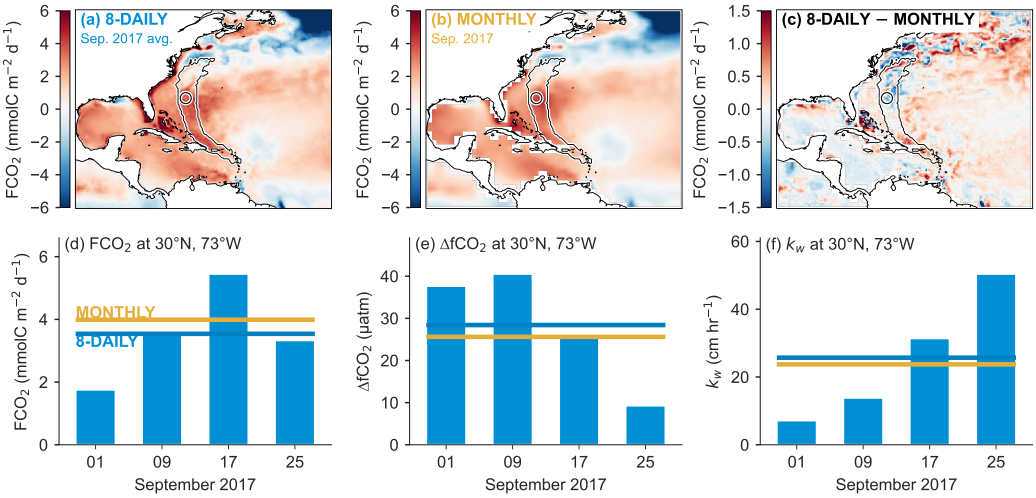

Figure 12. The mean of the 8-daily (a) and monthly (by) FCO_2 for September 2017. The contour line shows the path of Hurricane Maria from 17^{th} to 27^{th} September, where hourly winds exceeded 20 m s^{-1}. (c) the difference between the 8-daily mean and monthly values. (d) a bar plot of FCO_2 for the four time steps in September 2017 for the location indicated by the circle in the maps (a-c). (e) and (f) represent the same, but for $\Delta f CO_2$ and k_w respectively. The FCO_2 shown in (d) can be thought of as the product of the corresponding bars in (e) and (f) which are scaled by the solubility (not shown). Slight differences between averages (horizontal lines in e,f) are due to the marker not being at exactly the same location for high and low-resolution estimates.

the local-scale impacts of the increase in variance by assessing the FCO_2 during the passage of Maria, which represents a short-lasting extreme event that is missed in monthly reconstructions.

At first glance, the spatial distribution of the September 2017 mean of the 8D and 1M FCO_2 look similar (Figure 12a,b). However, the difference between the two mean states (Figure 12c) shows that outgassing was in fact less intense along the northern part of the hurricane path for the 8D FCO_2 relative to 1M. To better understand the lower-than-expected outgassing, we plot the temporal evolution of the fluxes, $\Delta f CO_2$ and k_w at a point location (29°N, 72°W) for each of the 8-daily time steps in September 2017 (Figure 12d-f). The location exhibits one of the strongest differences between the 8D and 1M FCO_2 for the spatio-temporal domain.

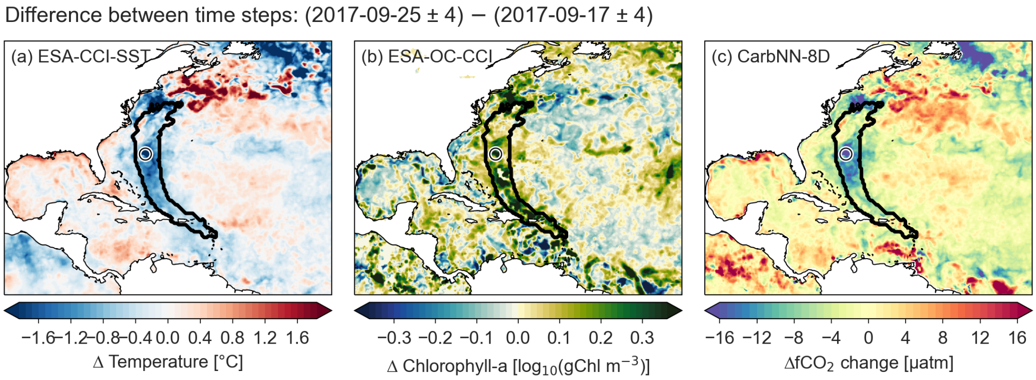

Figure 13. Maps showing the difference in (a) sea surface temperature, (b) chlorophyll-a, (c) ΔfCO_2 before and after Hurricane Maria in 2017. The two time periods are in September 13 – 20, and September 21 – 28. The black contour line shows the path of Hurricane Maria, defined by wind speeds > 20 m s^{-1}.

Importantly, we can also show that the response in Figure 12 is not just due to the intensification of the wind, but also due to changes in fCO$_2$ (Figure 12e,f). OceanCarbNN is able to capture a decrease in ΔfCO$_2$ from the period centered on the 17th to the following period on the 25th of September, particularly between $\sim$ 25°N to $\sim$ 30°N (Figure 13c). The decrease (> |15| µatm) co-occurs with a reduction in sea surface temperature and an increase in chlorophyll-a (Figure 13a,b), a relationship which has been previously observed (Babin et al., 2004; Reul et al., 2021).

Mechanistically, the decrease in fCO$_2$ is consistent with past studies that have found tropical cyclones to cool the surface ocean (decreasing fCO$_2$), but also inducing mixing that entrains carbon-rich waters, thus increasing fCO$_2$ (Yu et al., 2020). This is followed by an increase in primary productivity (i.e., a reduction in fCO$_2$ Babin et al., 2004; Lévy et al., 2012; Yu et al., 2020). For our point location, SST decreased by 2.6 °C between the two periods (Figure 12a), which would lead to a reduction in fCO$_2$ of $\sim$42 µatm. However, OceanCarbNN predicts a reduction of 24 µatm, leaving an excess of 18 µatm, which we attribute to the entrainment of DIC-rich waters. However, an increase in chlorophyll-a would result in a further decrease in fCO$_2$, meaning that the contribution of entrainment could be even larger; however, this contribution cannot be empirically determined.

While OceanCarbNN captures the impacts of Hurricane Maria on $F\mathrm{CO_2}$ and $f\mathrm{CO_2}$, the magnitude of the event is likely underestimated. For example, observation-based studies found that high-velocity winds increased outgassing by > 30 mmolC m^{-2} day^{-1} for $\sim$24 hrs (Yu et al., 2020; Ye et al., 2020), compared to the 2 mmolC m^{-2} day^{-1} increase observed from 9 to 17 September (Figure 12d). The 8D resolution averages out the short-lasting spikes ($\sim$24 hrs). Furthermore, satellite and reanalysis products may underestimate the spikes; for example, ERA5 underestimates extreme wind conditions by between 5–10% (relative to satellites Campos et al., 2022). Future work could address this by investigating the influence of using 8-daily $\Delta f\mathrm{CO_2}$ with hourly, daily, 8-daily and monthly k_w using an extreme wind speed specific wind speed dataset (e.g., `https://www.maxss.org`).

7 Discussion

We provide here for the first time a global-scale gap filled $f\mathrm{CO_2}$ product at an 8 daily and 0.25° × 0.25° resolution, from which we can compute the air-sea $\mathrm{CO_2}$ fluxes at the same unprecedented resolution. But what are we gaining from this increase in resolution in terms of quality and what are we learning from this in terms of processes? Next, we discuss these two questions in turn.

7.1 Does higher resolution reduce uncertainty in the mapping of $f\mathbf{CO_2}$?

In their work investigating a range of gap filled $f\mathrm{CO_2}$ products at 1M resolution, Gregor et al. (2019) found that all products had very similar RMSD estimates ranging between 15–20 µatm. They proposed that this is a methodological wall beyond which it would be difficult to progress. Our question is thus, can higher resolution get us over the wall?

In the open ocean, we find little to no reduction in the uncertainties, i.e., the RMSD of our 8D product in the open ocean ($\sim$13 µatm) is similar to that of the previous approaches at 1M resolution (Figure 3f). Further, relatively large biases still occur in some poorly-sampled regions (Figures 5 and 6). In the coastal ocean there is a some gain, with OceanCarbNN having a lower RMSD (25.4 µatm) relative to OceanSODA-ETHZ (27 µatm), a monthly by 1° $p\mathrm{CO_2}$-product (Gregor & Gruber, 2021). An improvement in the coastal ocean RMSD was also reported by Chau et al. (2024) in the CMEMS-FFNN approach

(28.5 µatm to 27.6 µatm) by increasing the spatial resolution from 1° to 0.25° (though not the temporal resolution). The slight reduction in coastal RMSD in both approaches is likely due to the fact that sharper gradients and fine-scale features are better represented in high-resolution estimates (e.g., Figure 8). In other words, there is better match-up between the gridded $f\mathrm{CO}_2$ observations and the gridded predictors, also called the representation uncertainty by (Gregor & Gruber, 2021).

Thus, while there is an improvement in the random uncertainties of the gap-filled $f\mathrm{CO}_2$ product at 8D resolution, this is not a breakthrough. Some further reduction may be achieved by going to even higher resolution, especially in time, as this would permit to capture the more ephemeral or faster developing features, such as the tropical instability waves and short-lived upwelling events. The big challenge here is the global-scale availability of predictor variables. The continuing development of global ocean reanalyses that also increasingly incorporate ocean color (e.g., Green Mercator) or commercial satellite observations at daily and 10 m spatial resolutions (Shutler et al., 2024) may soon provide such very high frequency predictors.

At the same time, we may be at the limit of the capability of the current generation of gap-filling methods that use simple architecture. With the current architecture, where each sample is independent in space and time, gap-filling methods need to solve two problems: 1) the basin-scale problem, where high accuracy of the inferred $f\mathrm{CO}_2$ is absolutely essential for constraining the ocean carbon sink, and 2) a fine-scale problem, where drivers can cause rapid and short spatial scales variations in $f\mathrm{CO}_2$ that need to be tracked with high precision. The challenge for the statistical methods is not simple, since similar changes in the drivers can have opposite effects on $f\mathrm{CO}_2$. A typical example occurs during El Niño phases in the eastern equatorial Pacific. Warm phases in this region typically go together with low $f\mathrm{CO}_2$ as a result of the cessation of upwelling (Feely et al., 1999). At the same time, a local heatwave would still push up $f\mathrm{CO}_2$. One option to explore is the use of multiscale methods that use information about the neighboring observations $f\mathrm{CO}_2$ or features (in space and time), such as those used for weather forecasting (e.g., GraphCast and FourCastNet; Lam et al., 2023; Pathak et al., 2022).

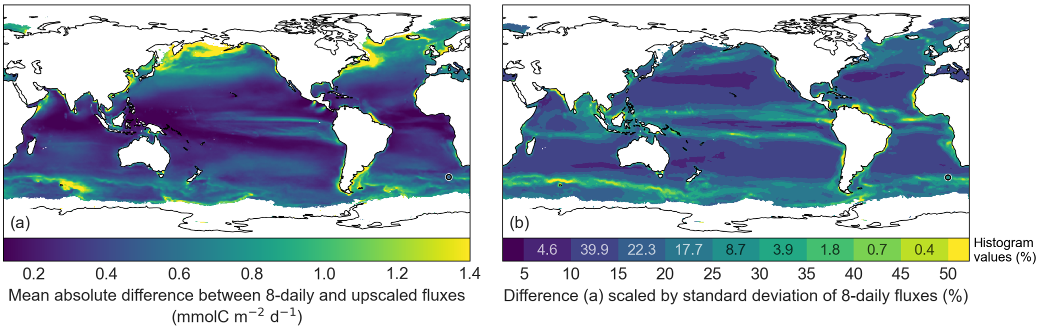

Figure 14. (a) The mean absolute difference (MAD) between $F\mathrm{CO}_2^{\mathrm{8D}}$ and $F\mathrm{CO}_2^{\mathrm{upscaled}}$, where the latter is calculated with k_x^{8D} and $\Delta f\mathrm{CO}_2^{\mathrm{1M}}$ upscaled to 8D. Thus, (a) shows the impact of using high resolution $\Delta f\mathrm{CO}_2$, even if a high resolution gas transfer velocity is used. (b) shows the MAD from (a) scaled to the standard deviation of the high resolution fluxes (Figure 9b). The values in the color bar represent the percentage cover that the histogram bin occupies in (b).

7.2 What do we learn from high resolution $F\mathrm{CO}_2$?

Our results show that there are distinct benefits of high resolution predictions of $f\mathrm{CO}_2$ and air-sea CO_2 flux. First, the high-resolution predictions of $f\mathrm{CO}_2$ reduce the uncertainty of the estimates relative to past low-resolution estimates in the coastal ocean due to improved match-ups between the in-situ target data (i.e., SOCAT) and the remote predictors (Section 7.1). And, the higher resolution captures more variability of $f\mathrm{CO}_2$ and air-sea CO_2 fluxes (Figure 11). However, we also show that the majority of the gained variability, particularly at the subseasonal scale, is due to an increase in the temporal resolution of wind represented by k_x.

Since winds drive the majority of the increase in variability, a key question is whether a similar result can be achieved by "upscaling" the fluxes. The upscaled fluxes ($F\mathrm{CO}_2^{\mathrm{upscaled}}$) are calculated using low-resolution $f\mathrm{CO}_2$ and high-resolution k_x. The difference between $F\mathrm{CO}_2^{\mathrm{8D}}$ and $F\mathrm{CO}_2^{\mathrm{upscaled}}$ (Figure 14a) quantifies the amount of information missed when relying solely on $F\mathrm{CO}_2^{\mathrm{upscaled}}$. In large parts of the ocean, particularly the gyre regions, we find minimal differences between $F\mathrm{CO}_2^{\mathrm{8D}}$ and $F\mathrm{CO}_2^{\mathrm{upscaled}}$ (< 0.4 mmolC m^{-2} d^{-1}, as shown in Figure 14a). However, in dynamic regions of the ocean, the differences can be substantial (> 1 mmolC m^{-2} d^{-1}).

Scaling these results by the standard deviation of $F\mathrm{CO}_2^{8\mathrm{D}}$ indicates the local importance of using the high resolution $F\mathrm{CO}_2$ (Figure 14b). The Antarctic Circumpolar Current (ACC) is the most striking feature, where significant additional variability is added due to the high resolution. Interestingly, this aligns with an observation-based study by in the Atlantic sector of the ACC that suggested a 3-daily sampling frequency of $f\mathrm{CO}_2$ is required to constrain fluxes to a 10% uncertainty threshold (location indicated by the marker in Figure 14; Monteiro et al., 2015). This also holds true for the eastern boundary upwelling regions, and the continental shelf regions in the high latitude Pacific and Atlantic. Thus, it is in regions where there is the combination of high spatio-temporal variability and high wind speeds that drivers the large differences between $F\mathrm{CO}_2^{8\mathrm{D}}$ and $F\mathrm{CO}_2^{\mathrm{upscaled}}$. However, it is also important to recognize that more sporadic events, such as Hurricane Maria, are also captured, but they may contribute little to the large-scale variability due to their short-lived nature (Lévy et al., 2012). While a step in the right direction, we also have to note that the magnitude of the variability is likely underestimated at the 8-daily resolution, e.g., Hurricane Maria (Lévy et al., 2012; Yu et al., 2020; Ye et al., 2020).

Despite the increases in local-scale variability, we do not see major differences between the mean air-sea CO_2 fluxes at 8-daily and monthly-resolutions at global and interannual scales (Figures 9a and 11). Thus, if the aim is to constrain $f\mathrm{CO}_2$ at a large scale, e.g., for the Global Carbon Budget (Friedlingstein et al., 2022), our analysis suggests that there is little reason to use 8-daily by 0.25° estimates. Importantly, increasing the resolution of $f\mathrm{CO}_2$ does not solve current unanswered problems and questions. For example, the growing divide in globally integrated $f\mathrm{CO}_2$ between the $f\mathrm{CO}_2$-products and Global Ocean Biogeochemical Models (GOBMs) over the last decade (2010−2022). Several studies have pinned this divergence on the overestimation of decadal variability by the $f\mathrm{CO}_2$-products (Gloege et al., 2021; Hauck et al., 2023), though the evidence is not conclusive, and it may be GOBMs that underestimate decadal variability (Mayot et al., 2023). However, the fact remains that $f\mathrm{CO}_2$-products suffer from observational paucity and sampling biases (Rödenbeck et al., 2015; Ritter et al., 2017; Gloege et al., 2021; Hauck et al., 2023), a problem that the high-resolution FOC_2 estimates presented here cannot solve.

8 Caveats

There are a number of specific caveats and challenges that need to be considered in our novel 8D product. The first concerns the use of the NOAA marine boundary layer product for the atmospheric dry air mixing ratio ($x\mathrm{CO}_2^{\mathrm{mbl}}$) for the computation of the air-sea CO_2 difference. The second concerns the use of a stacked salinity product in order to produce a high resolution product spanning four decades.

The use of the NOAA $x\mathrm{CO}_2^{\mathrm{mbl}}$ product most likely will underestimate the oceanic CO_2 uptake in regions downwind of the high anthropogenic CO_2 emission regions. This is because the NOAA $x\mathrm{CO}_2^{\mathrm{mbl}}$ product is constructed from marine stations primarily located in the Pacific Ocean, maximally away from any emissions. This contrasts with many regions in the North Atlantic, in the western Pacific, and close to the continents that are downstream of the major emitters and thus have substantially higher $x\mathrm{CO}_2$ than suggested by the marine boundary layer product (Leinweber et al., 2009). (Palter et al., 2023) recently pointed out that this effect can be quite substantial in the downwind regions, and suggested that this effect needs to be included in regional assessments. At the same time, they pointed out that this effect is negligible when the global ocean uptake is considered. Still, as we are pushing the oceanic $f\mathrm{CO}_2$ to higher resolution, we should also pay more attention to the spatio-temporal variations in atmospheric CO_2.

The second caveat concerns the difficulties associated with the estimation of $f\mathrm{CO}_2$ over a four decade period, given limitations in the availability of the predictors of choice (Figure 2). For chlorophyll and sea surface height, this means that climatologies are used for the periods where there is no coverage (prior to 1998 and 1993 respectively). Given that climatologies have smoother fields, the $f\mathrm{CO}_2$ estimates reflect this smoother input data. In the case of salinity, three different products are used over the four decade period (Figures 2, S3a).

The difference in variability between the salinity products can be large for some regions (e.g., Figure S3e). For the majority of the open ocean, the difference between salinity products does not make a significant difference, since salinity is a weak driver of $\Delta f\mathrm{CO}_2$ ($< |5|$ µatm PSU^{-1}; Figure S3a). However, in the equatorial Pacific, particularly in the western part of the basin, the sensitivity of $\Delta f\mathrm{CO}_2$ to salinity is large ($>$ 20 µatm PSU^{-1}). This means that salinity anomalies typically drive a change of more than ~ 10 µatm in the western equatorial Pacific for the SODA v3.4.2 salinity (Figure

S3b). For the ESA-CCI salinity, the salinity climate data record product, salinity drives an average change of ∼6 µatm.

We stress that this only impacts the variability of $\Delta f\mathrm{CO_2}$ since the mean state is captured by the 8-daily climatology of salinity. However, it does mean that variability of $f\mathrm{CO_2}$ in the western equatorial Pacific, may be overestimated in the period 1982-1992 (SODA salinity) and underestimated from 1993-2009 (CMEMS-Multiobs). This applies particularly to the large-scale changes in salinity driven by El Niño. While this is a lesser problem for $\Delta f\mathrm{CO_2}$ predictions, this will have a much stronger influence on machine learning estimates of total alkalinity (e.g., Gregor & Gruber, 2021)

9 Conclusions and next steps

In this study, we present the first 8-daily by 0.25° × 0.25° estimates of air-sea $\mathrm{CO_2}$ fluxes at a global scale over four decades. The high-resolution pCO2-product, OceanCarbNN, is able to capture significantly more variability in air-sea $\mathrm{CO_2}$ flux, with the majority of the increased variability is driven by higher resolution winds, rather than $f\mathrm{CO_2}$. However, we also show that high resolution $f\mathrm{CO_2}$ is important in regions with high variability. This includes short-lived high intensity events such as upwelling events and hurricanes.

Following the approach of (Gregor & Gruber, 2021), the $f\mathrm{CO_2}$ estimates from the OceanCarbNN approach can be combined with high resolution estimates of total alkalinity to estimate high resolution ocean acidification parameters that could be used to better understand ocean acidification extremes, for example (Gruber et al., 2021; Desmet et al., 2022; Burger et al., 2020). Understanding such extreme events from historical data is important so that the drivers of extremes can be better characterized (Gruber et al., 2021). This then also allows us to understand current extreme events, such as the North Atlantic marine heatwave in 2023, that could drive anomalous changes in ocean acidification. This requires near real-time capability of machine learning approaches, which is technically quite feasible. However, the current release cycle of SOCAT means that near-real time estimates would be predicting up to 1.5 years beyond the target data (D. C. Bakker et al., 2016). The impact of predicting beyond the target data needs to be investigated before results can be used.

Another area of improvement lies in the temporal resolution of our air-sea CO_2 fluxes. The psuedo-daily estimates of air-sea CO_2 fluxes could quite simply be estimated by up-scaling $\Delta f\mathrm{CO}_2$ to daily resolution while using daily estimates of k_w. This could be further improved by using daily predictors for those that are available (e.g., SST, and SSH) alongside upscaled predictors for those that are not. However, the gain from 8-daily to daily $f\mathrm{CO}_2$ at the current spatial resolution (0.25°) is unlikely to be as large as the improvement from monthly to 8-daily (Monteiro et al., 2015).

Finally, the field of machine learning is developing at an unprecedented rate. New approaches such as Fourier neural operators used in Nvidia's FourcastNet could be incorporated to better capture fine-scale variability of $f\mathrm{CO}_2$. However, it is unclear if even these approaches would be able to reduce the uncertainties beyond "the wall" that sits between 15 and 20 µatm.

10 Open Research

The OceanCarbNN dataset of $\Delta f\mathrm{CO}_2$ and $F\mathrm{CO}_2$ produced and used throughout this study are available at `https://data.up.ethz.ch/shared/ESA-OHOA/OceanSODA_ETHZ_HR-v2023.01-full_carbsys/` (this will change to a repository with a DOI once publication is accepted). Code to create the OceanCarbNN data is hosted on `https://gitlab.ethz.ch/oceansoda/oceancarbnn` and code for the study analysis and figures are hosted at `https://gitlab.ethz.ch/oceansoda/gbc-gregor-et-al-high-res-variability-fco2` (A DOI will be given to the code repositories once the publication is accepted). All data used to create the abovementioned dataset are at least open-access under academic license and are listed here. SOCAT v2023 data was downloaded from `https://socat.info/socat_files/v2023/SOCATv2023.tsv.zip` (D. C. Bakker et al., 2016; D. C. E. Bakker et al., 2023). Sea surface temperature is from `https://doi.org/10.48670/moi-00169` (Good et al., 2020). ERA5 data (wind and sea level pressure) are from `https://doi.org/10.24381/cds.adbb2d47` (Hersbach et al., 2020, 2023). Salinity from 2010-2020 is from `https://catalogue.ceda.ac.uk/uuid/fad2e982a59d44788eda09e3c67ed7d5` (Boutin et al., 2021). Salinity and mixed layer depth from SODA v3.4.2 were downloaded from `https://dsrs.atmos.umd.edu/DATA/soda3.4.2/REGRIDED/ocean/` (Carton et al., 2018). Salinity after 2021 was downloaded from `https://doi.org/10.48670/moi-00051` (Droghei et al., 2016). Chlorophyll-a data can be found at `https://www.oceancolour.org/` (Sathyendranath et al., 2023). We used the reprocessed sea surface height from `https://doi.org/10.48670/moi-00148` (see acknowledgements).

References

Abadi, M., Agarwal, A., Barham, P., Brevdo, E., Chen, Z., Citro, C., ... Zheng, X. (2015). *TensorFlow: Large-scale machine learning on heterogeneous systems.* Retrieved from `https://www.tensorflow.org/` (Software available from tensorflow.org)

Alvera-Azcárate, A., Barth, A., Sirjacobs, D., Lenartz, F., & Beckers, J. M. (2011). Data interpolating empirical orthogonal functions (DINEOF): A tool for geophysical data analyses. *Mediterranean Marine Science*, *12*(3), 5–11. doi: 10.12681/mms.64

Arruda, R., Calil, P. H. R., Bianchi, A. A., Doney, S. C., Gruber, N., Lima, I., & Turi, G. (2015). Air-sea CO_2 fluxes and the controls on ocean surface pCO_2 seasonal variability in the coastal and open-ocean southwestern Atlantic Ocean: A modeling study. *Biogeosciences*, *12*(19), 5793–5809. doi: 10.5194/bg-12-5793-2015

Babin, S. M., Carton, J. A., Dickey, T. D., & Wiggert, J. D. (2004). Satellite evidence of hurricane-induced phytoplankton blooms in an oceanic desert. *Journal of Geophysical Research: Oceans*, *109*(C3). doi: 10.1029/2003JC001938

Bakker, D. C., Pfeil, B., Landa, C. S., Metzl, N., O'Brien, K. M., Olsen, A., ... Xu, S. (2016). A multi-decade record of high-quality fCO2 data in version 3 of the Surface Ocean CO2 Atlas (SOCAT). *Earth System Science Data*, *8*(2), 383–413. doi: 10.5194/essd-8-383-2016

Bakker, D. C. E., Alin, S. R., Bates, N., Becker, M., Feely, R. A., Gkritzalis, T., ... Wimart-Rousseau, C. (2023). *Surface ocean CO2 atlas database version 2023 (SOCATv2023) (NCEI accession 0278913).* NOAA National Centers for Environmental Information. doi: 10.25921/r7xa-bt92

Bates, N. R., Astor, Y. M., Church, M. J., Currie, K., Dore, J. E., González-Dávila, M., ... Santana-Casiano, J. M. (2014). A time-series view of changing surface ocean chemistry due to ocean uptake of anthropogenic CO2 and ocean acidification. *Oceanography*, *27*(1), 126–141. doi: 10.5670/oceanog.2014.16

Bates, N. R., Takahashi, T., Chipman, D. W., & Knap, A. H. (1998). Variability of pCO2 on diel to seasonal timescales in the Sargasso Sea near Bermuda. *Journal of Geophysical Research: Oceans*, *103*(C8), 15567–15585. doi: 10.1029/98JC00247

Bennington, V., Galjanic, T., & McKinley, G. A. (2022). Explicit Physical Knowledge in Machine Learning for Ocean Carbon Flux Reconstruction: The pCO2-Residual Method. *Journal of Advances in Modeling Earth Systems*, *14*(10). doi: 10.1029/2021MS002960

Boutin, J., Merlivat, L., HÉnocq, C., Martin, N., & SallÉe, J. B. (2008). Air-sea CO2 flux variability in frontal regions of the Southern Ocean from CARbon Interface OCean Atmosphere drifters. *Limnology and Oceanography*, *53*(5part2), 2062–2079. doi: 10.4319/lo.2008.53.5_part_2.2062

Boutin, J., Vergely, J. L., Marchand, S., D'Amico, F., Hasson, A., Kolodziejczyk, N., … Vialard, J. (2018). New SMOS Sea Surface Salinity with reduced systematic errors and improved variability. *Remote Sensing of Environment*, *214*(August 2017), 115–134. doi: 10.1016/j.rse.2018.05.022

Boutin, J., Vergely, J.-L., Reul, N., Catany, R., Koehler, J., Martin, A., … Donlon, C. (2021). *ESA Sea Surface Salinity Climate Change Initiative (Sea_Surface_Salinity_cci): Weekly sea surface salinity product, v03.21, for 2010 to 2020.* NERC EDS Centre for Environmental Data Analysis. Retrieved Accessed on 21-02-2023, from `\url{https://catalogue.ceda.ac.uk/uuid/fad2e982a59d44788eda09e3c67ed7d5}`

Burger, F. A., John, J. G., & Frölicher, T. L. (2020). Increase in ocean acidity variability and extremes under increasing atmospheric CO2. *Biogeosciences*, *17*(18), 4633–4662. doi: 10.5194/bg-17-4633-2020

Burt, W. J., Thomas, H., Miller, L. A., Granskog, M. A., Papakyriakou, T. N., & Pengelly, L. (2016). Inorganic carbon cycling and biogeochemical processes in an Arctic inland sea (Hudson Bay). *Biogeosciences*, *13*(16), 4659–4671. doi: 10.5194/BG-13-4659-2016

Campos, R. M., Gramcianinov, C. B., de Camargo, R., & da Silva Dias, P. L. (2022). Assessment and Calibration of ERA5 Severe Winds in the Atlantic Ocean Using Satellite Data. *Remote Sensing*, *14*(19), 4918. doi: 10.3390/rs14194918

Carton, J. A., Chepurin, G. A., & Chen, L. (2018). SODA3: A new ocean climate reanalysis. *Journal of Climate*, *31*(17), 6967–6983. doi: 10.1175/JCLI-D-17-0149.1

Chapa-Balcorta, C., Hernandez-Ayon, J. M., Durazo, R., Beier, E., Alin, S. R., & López-Pérez, A. (2015). Influence of post-Tehuano oceanographic processes in the dynamics of the CO2 system in the Gulf of Tehuantepec, Mexico. *Journal of Geophysical Research: Oceans*, *120*(12), 7752–7770. doi: 10.1002/2015JC011249

Chau, T. T. T., Gehlen, M., & Chevallier, F. (2022). A seamless ensemble-based reconstruction of surface ocean pCO2 and air-sea CO2 fluxes over the global coastal and open oceans. *Biogeosciences*, *19*(4), 1087–1109. doi: 10.5194/bg-19-1087-2022

Chau, T.-T.-T., Gehlen, M., Metzl, N., & Chevallier, F. (2024). CMEMS-LSCE: A global, 0.25°, monthly reconstruction of the surface ocean carbonate system. *Earth System Science Data*, *16*(1), 121–160. doi: 10.5194/essd-16-121-2024

Chen, S., Hu, C., Barnes, B. B., Wanninkhof, R., Cai, W.-J., Barbero, L., & Pierrot, D. (2019). A machine learning approach to estimate surface ocean pCO2 from satellite measurements. *Remote Sensing of Environment*, *228*, 203–226. doi: 10.1016/j.rse.2019.04.019

Courtois, A., Morel, J. M., & Arias, P. (2023). Can neural networks extrapolate? Discussion of a theorem by Pedro Domingos. *Revista de la Real Academia de Ciencias Exactas, Fisicas y Naturales - Serie A: Matematicas*, *117*(2), 1–26. doi: 10.1007/s13398-023-01411-z

Denvil-Sommer, A., Gehlen, M., Vrac, M., & Mejia, C. (2019). LSCE-FFNN-v1: A two-step neural network model for the reconstruction of surface ocean p CO 2 over the global ocean. *Geoscientific Model Development*, *12*(5), 2091–2105. doi: 10.5194/gmd-12-2091-2019

Desmet, F., Gruber, N., Köhn, E. E., Münnich, M., & Vogt, M. (2022). Tracking the Space-Time Evolution of Ocean Acidification Extremes in the California Current System and Northeast Pacific. *Journal of Geophysical Research: Oceans*, *127*(5), e2021JC018159. doi: 10.1029/2021JC018159

DeVries, T., Le Quéré, C., Andrews, O., Berthet, S., Hauck, J., Ilyina, T., ... Séférian, R. (2019). Decadal trends in the ocean carbon sink. *Proceedings of the National Academy of Sciences*, *116*(24), 201900371. doi:

10.1073/pnas.1900371116

DeVries, T., Yamamoto, K., Wanninkhof, R., Gruber, N., Hauck, J., Müller, J. D., … Zeng, J. (2023). Magnitude, trends, and variability of the global ocean carbon sink from 1985-2018. *Global Biogeochemical Cycles*, e2023GB007780. doi: 10.1029/2023GB007780

Dlugokencky, E., Thoning, K., Lan, X., & Tans, P. (2021). *NOAA Greenhouse Gas Reference from Atmospheric Carbon Dioxide Dry Air Mole Fractions from the NOAA GML Carbon Cycle Cooperative Global Air Sampling Network.*

Doney, S. C., Lima, I., Feely, R. A., Glover, D. M., Lindsay, K., Mahowald, N., … Wanninkhof, R. H. (2009). Mechanisms governing interannual variability in upper-ocean inorganic carbon system and air–sea CO2 fluxes: Physical climate and atmospheric dust. *Deep Sea Research Part II: Topical Studies in Oceanography*, *56*(8-10), 640–655. doi: 10.1016/j.dsr2.2008.12.006

Droghei, R., Buongiorno Nardelli, B., & Santoleri, R. (2016). Combining in situ and satellite observations to retrieve salinity and density at the ocean surface. *Journal of Atmospheric and Oceanic Technology*, *33*(6), 1211–1223. doi: 10.1175/JTECH-D-15-0194.1

Fay, A. R., Gregor, L., Landschützer, P., McKinley, G. A., Gruber, N., Gehlen, M., … Zeng, J. (2021). SeaFlux: Harmonization of air–sea CO2 fluxes from surface pCO2 data products using a standardized approach. *Earth System Science Data*, *13*(10), 4693–4710. doi: 10.5194/essd-13-4693-2021

Fay, A. R., & McKinley, G. A. (2014). Global open-ocean biomes: Mean and temporal variability. *Earth System Science Data*, *6*(2), 273–284. doi: 10.5194/essd-6-273-2014

Feely, R. A., Wanninkhof, R., Takahashi, T., & Tans, P. (1999). Influence of El Niño on the equatorial Pacific contribution to atmospheric CO2 accumulation. *Nature*, *398*(6728), 597–601. doi: 10.1038/19273

Friederich, G. E., Ledesma, J., Ulloa, O., & Chavez, F. P. (2008). Air–sea carbon dioxide fluxes in the coastal southeastern tropical Pacific. *Progress in Oceanography*, *79*(2), 156–166. doi: 10.1016/j.pocean.2008.10.001

Friederich, G. E., Walz, P. M., Burczynski, M. G., & Chavez, F. P. (2002). Inorganic carbon in the central California upwelling system during the 1997-1999 El Niño-La Niña event. *Progress in Oceanography*, *54*(1-4), 185–203. doi:

10.1016/S0079-6611(02)00049-6

Friedlingstein, P., O'Sullivan, M., Jones, M. W., Andrew, R. M., Bakker, D. C. E., Hauck, J., ... Zheng, B. (2023). Global Carbon Budget 2023. *Earth System Science Data*, *15*(12), 5301–5369. doi: 10.5194/essd-15-5301-2023

Friedlingstein, P., O'Sullivan, M., Jones, M. W., Andrew, R. M., Gregor, L., Hauck, J., ... Zheng, B. (2022). Global Carbon Budget 2022. *Earth System Science Data*, *14*(11), 4811–4900. doi: 10.5194/essd-14-4811-2022

Fukushima, K. (1969). Visual Feature Extraction by a Multilayered Network of Analog Threshold Elements. *IEEE Transactions on Systems Science and Cybernetics*, *5*(4), 322–333. doi: 10.1109/TSSC.1969.300225

Gade, K. (2010). A Non-singular Horizontal Position Representation. *Journal of Navigation*, *63*(03), 395–417. doi: 10.1017/S0373463309990415

Gloege, L., McKinley, G. A., Landschützer, P., Fay, A. R., Frölicher, T. L., Fyfe, J. C., ... Takano, Y. (2021). Quantifying Errors in Observationally Based Estimates of Ocean Carbon Sink Variability. *Global Biogeochemical Cycles*, *35*(4), 1–14. doi: 10.1029/2020GB006788

Gloege, L., Yan, M., Zheng, T., & McKinley, G. A. (2022). Improved Quantification of Ocean Carbon Uptake by Using Machine Learning to Merge Global Models and pCO2 Data. *Journal of Advances in Modeling Earth Systems*, *14*(2), 1–19. doi: 10.1029/2021MS002620

González, M. F., & Ilyina, T. (2016). Impacts of artificial ocean alkalinization on the carbon cycle and climate in Earth system simulations. *Geophysical Research Letters*, *43*(12), 6493–6502. doi: 10.1002/2016GL068576

Good, S. A., Fiedler, E., Mao, C., Martin, M. J., Maycock, A., Reid, R., ... Worsfold, M. (2020). The current configuration of the OSTIA system for operational production of foundation sea surface temperature and ice concentration analyses. *Remote Sensing*, *12*(4), 1–20. doi: 10.3390/rs12040720

Goyet, C., Bradshaw, A. L., & Brewer, P. G. (1991). The carbonate system in the Black Sea. *Deep Sea Research Part A. Oceanographic Research Papers*, *38*(Suppl. 2A), S1049-S1068. doi: 10.1016/S0198-0149(10)80023-8

Gregor, L., & Gruber, N. (2021). OceanSODA-ETHZ: A global gridded data set of the surface ocean carbonate system for seasonal to decadal studies of ocean acidification. *Earth System Science Data*, *13*(2), 777–808. doi:

10.5194/essd-13-777-2021

Gregor, L., Lebehot, A. D., Kok, S., & Scheel Monteiro, P. M. (2019). A comparative assessment of the uncertainties of global surface ocean CO2 estimates using a machine-learning ensemble (CSIR-ML6 version 2019a) - have we hit the wall? *Geoscientific Model Development*, *12*(12), 5113–5136. doi: 10.5194/gmd-12-5113-2019

Gruber, N., Bakker, D. C. E., DeVries, T., Gregor, L., Hauck, J., Landschützer, P., ... Müller, J. D. (2023). Trends and variability in the ocean carbon sink. *Nature Reviews Earth & Environment*, *4*(2), 119–134. doi: 10.1038/s43017-022-00381-x

Gruber, N., Boyd, P. W., Frölicher, T. L., & Vogt, M. (2021). Biogeochemical extremes and compound events in the ocean. *Nature*, *600*(7889), 395–407. doi: 10.1038/s41586-021-03981-7

Gruber, N., Clement, D., Carter, B. R., Feely, R. A., van Heuven, S., Hoppema, M., ... Wanninkhof, R. H. (2019). The oceanic sink for anthropogenic CO 2 from 1994 to 2007. *Science*, *363*(6432), 1193–1199. doi: 10.1126/science.aau5153

Gruber, N., Landschützer, P., & Lovenduski, N. S. (2019). The Variable Southern Ocean Carbon Sink. *Annual Review of Marine Science*, *11*(1), 159–186. doi: 10.1146/annurev-marine-121916-063407

Gu, Y., Katul, G. G., & Cassar, N. (2023). Multiscale Temporal Variability of the Global Air-Sea CO 2 Flux Anomaly. *Journal of Geophysical Research: Biogeosciences*, *128*(6). doi: 10.1029/2022JG006934

Hauck, J., Nissen, C., Landschützer, P., Rödenbeck, C., Bushinsky, S., & Olsen, A. (2023). Sparse observations induce large biases in estimates of the global ocean CO2 sink: An ocean model subsampling experiment. *Philosophical Transactions of the Royal Society A: Mathematical, Physical and Engineering Sciences*, *381*(2249). doi: 10.1098/rsta.2022.0063

Hersbach, H., Bell, B., Berrisford, P., Biavati, G., Horányi, A., Muñoz Sabater, J., ... Thépaut, J.-N. (2023). *Era5 hourly data on single levels from 1940 to present.* Copernicus Climate Change Service (C3S) Climate Data Store (CDS). doi: 10.24381/cds.adbb2d47

Hersbach, H., Bell, B., Berrisford, P., Hirahara, S., Horányi, A., Muñoz-Sabater, J., ... Thépaut, J.-N. (2020). The ERA5 global reanalysis. *Quarterly Journal of* *the Royal Meteorological Society*, *146*(730), 1999–2049. doi: 10.1002/qj.3803

Holder, C., & Gnanadesikan, A. (2021). Can machine learning extract the mechanisms controlling phytoplankton growth from large-scale observations?-A proof-of-concept study. *Biogeosciences*, *18*(6), 1941–1970. doi: 10.5194/BG-18-1941-2021

Iida, Y., Takatani, Y., Kojima, A., & Ishii, M. (2021). Global trends of ocean CO2 sink and ocean acidification: An observation-based reconstruction of surface ocean inorganic carbon variables. *Journal of Oceanography*, *77*(2). doi: 10.1007/s10872-020-00571-5

Jähne, B., Heinz, G., & Dietrich, W. (1987). Measurement of the diffusion coefficients of sparingly soluble gases in water. *Journal of Geophysical Research*, *92*(C10), 10767. doi: 10.1029/JC092iC10p10767

Jones, S. D., Le Quéré, C., & Rdenbeck, C. (2012). Autocorrelation characteristics of surface ocean pCO2 and air-sea CO2 fluxes. *Global Biogeochemical Cycles*, *26*(2), 1–12. doi: 10.1029/2010GB004017

Ke, G., Meng, Q., Finley, T., Wang, T., Chen, W., Ma, W., . . . Liu, T.-Y. (2017). LightGBM: A highly efficient gradient boosting decision tree. In *Proceedings of the 31st International Conference on Neural Information Processing Systems* (pp. 3149–3157). Red Hook, NY, USA: Curran Associates Inc.

Khatiwala, S., Tanhua, T., Mikaloff Fletcher, S. E., Gerber, M., Doney, S. C., Graven, H. D., . . . Sabine, C. L. (2013). Global ocean storage of anthropogenic carbon. *Biogeosciences*, *10*(4), 2169–2191. doi: 10.5194/bg-10-2169-2013

Koch, J., McKinley, G. A., Bennington, V., & Ullman, D. (2009). Do hurricanes cause significant interannual variability in the air-sea CO2 flux of the subtropical North Atlantic? *Geophysical Research Letters*, *36*(7). doi: 10.1029/2009GL037553

Lachkar, Z., & Gruber, N. (2013). Response of biological production and air-sea CO2 fluxes to upwelling intensification in the California and Canary Current Systems. *Journal of Marine Systems*, *109–110*, 149–160. doi: 10.1016/j.jmarsys.2012.04.003

Lam, R., Sanchez-Gonzalez, A., Willson, M., Wirnsberger, P., Fortunato, M., Alet, F., . . . Battaglia, P. (2023). Learning skillful medium-range global weather forecasting. *Science*, *382*(6677), 1416–1421. doi: 10.1126/science.adi2336

Landschützer, P., Gruber, N., & Bakker, D. C. (2016). Decadal variations and trends of the global ocean carbon sink. *Global Biogeochemical Cycles*, *30*(10), 1396–1417. doi: 10.1002/2015GB005359

Landschützer, P., Gruber, N., Bakker, D. C., Schuster, U., Nakaoka, S., Payne, M. R., ... Zeng, J. (2013). A neural network-based estimate of the seasonal to inter-annual variability of the Atlantic Ocean carbon sink. *Biogeosciences*, *10*(11), 7793–7815. doi: 10.5194/bg-10-7793-2013

Landschützer, P., Gruber, N., Bakker, D. C., Stemmler, I., & Six, K. D. (2018). Strengthening seasonal marine CO2 variations due to increasing atmospheric CO2. *Nature Climate Change*, *8*(February), 146–150. doi: 10.1038/s41558-017-0057-x

Landschützer, P., Gruber, N., Haumann, F. A., Rödenbeck, C., Bakker, D. C., van Heuven, S., ... Wanninkhof, R. H. (2015). The reinvigoration of the Southern Ocean carbon sink. *Science*, *349*(6253), 1221–1224. doi: 10.1126/science.aab2620

Laruelle, G. G., Landschützer, P., Gruber, N., Ti, J. L., Delille, B., Regnier, P. A., & Tison, J.-L. (2017). Global high-resolution monthly pCO2 climatology for the coastal ocean derived from neural network interpolation. *Biogeosciences*, *14*(19), 4545–4561. doi: 10.5194/bg-14-4545-2017

Legeckis, R. (1977). Long Waves in the Eastern Equatorial Pacific Ocean: A View from a Geostationary Satellite. *Science*, *197*(4309), 1179–1181. doi: 10.1126/science.197.4309.1179

Leinweber, A., Gruber, N., Frenzel, H., Friederich, G. E., & Chavez, F. P. (2009). Diurnal carbon cycling in the surface ocean and lower atmosphere of Santa Monica Bay, California. *Geophysical Research Letters*, *36*(8). doi: 10.1029/2008GL037018

Lenton, A., Matear, R. J., Keller, D. P., Scott, V., & Vaughan, N. E. (2018). Assessing carbon dioxide removal through global and regional ocean alkalinization under high and low emission pathways. *Earth System Dynamics*, *9*(2), 339–357. doi: 10.5194/esd-9-339-2018

Lévy, M., Lengaigne, M., Bopp, L., Vincent, E. M., Madec, G., Ethé, C., ... Sarma, V. V. (2012). Contribution of tropical cyclones to the air-sea CO 2 flux: A global view. *Global Biogeochemical Cycles*, *26*(2). doi:

10.1029/2011GB004145

Liang, J.-H., McWilliams, J. C., & Gruber, N. (2009). High-frequency response of the ocean to mountain gap winds in the northeastern tropical Pacific. *Journal of Geophysical Research: Oceans*, *114*(C12). doi: 10.1029/2009JC005370

Ma, D., Gregor, L., & Gruber, N. (2023). Four Decades of Trends and Drivers of Global Surface Ocean Acidification. *Global Biogeochemical Cycles*, *37*(7). doi: 10.1029/2023GB007765

Mayot, N., Le Quéré, C., Rödenbeck, C., Bernardello, R., Bopp, L., Djeutchouang, L. M., ... Zeng, J. (2023). Climate-driven variability of the Southern Ocean CO 2 sink. *Philosophical Transactions of the Royal Society A: Mathematical, Physical and Engineering Sciences*, *381*(2249). doi: 10.1098/rsta.2022.0055

McKinley, G. A., Fay, A. R., Eddebbar, Y. A., Gloege, L., & Lovenduski, N. S. (2020). External Forcing Explains Recent Decadal Variability of the Ocean Carbon Sink. *AGU Advances*, *1*(2), e2019AV000149. doi: 10.1029/2019AV000149

Merchant, C. J., Embury, O., Bulgin, C. E., Block, T., Corlett, G. K., Fiedler, E., ... Donlon, C. J. (2019). Satellite-based time-series of sea-surface temperature since 1981 for climate applications. *Scientific data*, *6*(1), 223. doi: 10.1038/s41597-019-0236-x

Merlivat, L., Gonzalez Davila, M., Caniaux, G., Boutin, J., & Reverdin, G. (2009). Mesoscale and diel to monthly variability of CO2 and carbon fluxes at the ocean surface in the northeastern Atlantic. *Journal of Geophysical Research: Oceans*, *114*(C3). doi: 10.1029/2007JC004657

Mignot, A., von Schuckmann, K., Landschützer, P., Gasparin, F., van Gennip, S., Perruche, C., ... Amm, T. (2022). Decrease in air-sea CO2 fluxes caused by persistent marine heatwaves. *Nature Communications*, *13*(1), 4300. doi: 10.1038/s41467-022-31983-0

Monteiro, P. M. S., Gregor, L., Lévy, M., Maenner, S., Sabine, C. L., & Swart, S. (2015). Intraseasonal variability linked to sampling alias in air-sea CO2 fluxes in the Southern Ocean. *Geophysical Research Letters*, *42*(20), 8507–8514. doi: 10.1002/2015GL066009

Müller, J. D., Gruber, N., Carter, B., Feely, R., Ishii, M., Lange, N., ... Zhu, D. (2023). Decadal Trends in the Oceanic Storage of Anthropogenic

Carbon From 1994 to 2014. *AGU Advances*, *4*(4), e2023AV000875. doi: 10.1029/2023AV000875

Müller, J. D., Schneider, B., & Rehder, G. (2016). Long-term alkalinity trends in the Baltic Sea and their implications for CO2-induced acidification. *Limnology and Oceanography*, *61*(6), 1984–2002. doi: 10.1002/lno.10349

Murphy, P. P., Nojiri, Y., Harrison, D. E., & Larkin, N. K. (2001). Scales of spatial variability for surface ocean pCO2 in the Gulf of Alaska and Bering Sea: Toward a sampling strategy. *Geophysical Research Letters*, *28*(6), 1047–1050. doi: 10.1029/2000GL012375

Naegler, T. (2009). Reconciliation of excess 14C-constrained global CO2 piston velocity estimates. *Tellus, Series B: Chemical and Physical Meteorology*, *61 B*(2), 372–384. doi: 10.1111/j.1600-0889.2008.00408.x

Nicholson, S. A., Whitt, D. B., Fer, I., du Plessis, M. D., Lebéhot, A. D., Swart, S., ... Monteiro, P. M. (2022). Storms drive outgassing of CO2 in the subpolar Southern Ocean. *Nature Communications*, *13*(1), 1–12. doi: 10.1038/s41467-021-27780-w

Palter, J. B., Nickford, S., & Mu, L. (2023). Ocean Carbon Dioxide Uptake in the Tailpipe of Industrialized Continents. *Geophysical Research Letters*, *50*(21), e2023GL104822. doi: 10.1029/2023GL104822

Pardo, P. C., Tilbrook, B., van Ooijen, E., Passmore, A., Neill, C., Jansen, P., ... Trull, T. W. (2019). Surface ocean carbon dioxide variability in South Pacific boundary currents and Subantarctic waters. *Scientific Reports*, *9*(1), 7592. doi: 10.1038/s41598-019-44109-2

Pathak, J., Subramanian, S., Harrington, P., Raja, S., Chattopadhyay, A., Mardani, M., ... Anandkumar, A. (2022). *FourCastNet: A Global Data-driven High-resolution Weather Model using Adaptive Fourier Neural Operators* (No. arXiv:2202.11214). arXiv. doi: 10.48550/arXiv.2202.11214

Regnier, P. A., Resplandy, L., Najjar, R. G., & Ciais, P. (2022). The land-to-ocean loops of the global carbon cycle. *Nature 2022 603:7901*, *603*(7901), 401–410. doi: 10.1038/s41586-021-04339-9

Resplandy, L., Hogikyan, A., Müller, J. D., Najjar, R. G., Bange, H. W., Bianchi, D., ... Regnier, P. (2024). A Synthesis of Global Coastal Ocean Greenhouse Gas Fluxes. *Global Biogeochemical Cycles*, *38*(1), e2023GB007803. doi:

10.1029/2023GB007803

Reul, N., Chapron, B., Grodsky, S. A., Guimbard, S., Kudryavtsev, V., Foltz, G. R., & Balaguru, K. (2021). Satellite Observations of the Sea Surface Salinity Response to Tropical Cyclones. *Geophysical Research Letters*, *48*(1), e2020GL091478. doi: 10.1029/2020GL091478

Ritter, R., Landschützer, P., Gruber, N., Fay, A. R., Iida, Y., Jones, S. D., ... Zeng, J. (2017). Observation-Based Trends of the Southern Ocean Carbon Sink. *Geophysical Research Letters*, *44*(24), 12,339–12,348. doi: 10.1002/2017GL074837

Rödenbeck, C., Bakker, D. C., Gruber, N., Iida, Y., Jacobson, A. R., Jones, S. D., ... Zeng, J. (2015). Data-based estimates of the ocean carbon sink variability - first results of the surface ocean pco2 mapping intercomparison (SOCOM). *Biogeosciences*, *12*(23), 7251–7278. doi: 10.5194/bg-12-7251-2015

Rödenbeck, C., Bakker, D. C., Metzl, N., Olsen, A., Sabine, C. L., Cassar, N., ... Heimann, M. (2014). Interannual sea–air CO2 flux variability from an observation-driven ocean mixed-layer scheme. *Biogeosciences*, *11*(17), 4599–4613. doi: 10.5194/bg-11-4599-2014

Rödenbeck, C., DeVries, T., Hauck, J., Le Quéré, C., & Keeling, R. F. (2022). Data-based estimates of interannual sea–air CO_2 flux variations 1957–2020 and their relation to environmental drivers. *Biogeosciences*, *19*(10), 2627–2652. doi: 10.5194/bg-19-2627-2022

Rodgers, K. B., Schwinger, J., Fassbender, A. J., Landschützer, P., Yamaguchi, R., Frenzel, H., ... Velo, A. (2023). Seasonal Variability of the Surface Ocean Carbon Cycle: A Synthesis. *Global Biogeochemical Cycles*, *37*(9), e2023GB007798. doi: 10.1029/2023GB007798

Romero-Centeno, R., Zavala-Hidalgo, J., Gallegos, A., & O'Brien, J. J. (2003). Isthmus of Tehuantepec Wind Climatology and ENSO Signal. *Journal of Climate*, *16*(15), 2628–2639. doi: 10.1175/1520-0442(2003)016⟨2628:IOTWCA⟩2.0.CO;2

Roobaert, A., Regnier, P., Landschützer, P., & Laruelle, G. G. (2023). A novel sea surface pCO_2-product for the global coastal ocean resolving trends over the 1982–2020 period. *Earth System Science Data Discussions*, 1–32. doi: 10.5194/essd-2023-228

Sabine, C. L., Feely, R. A., Gruber, N., Key, R. M., Lee, K., Bullister, J. L., ...

Rios, A. F. (2004). The Oceanic Sink for Anthropogenic CO2. *Science*, *305*(5682), 367–371. doi: 10.1126/science.1097403

Sabine, C. L., Hankin, S., Koyuk, H., Bakker, D. C., Pfeil, B., Olsen, A., … Yoshikawa-Inoue, H. (2013). Surface Ocean CO2 Atlas (SOCAT) gridded data products. *Earth System Science Data*, *5*(1), 145–153. doi: 10.5194/essd-5-145-2013

Sarmiento, J. L., & Gruber, N. (2006). *Ocean Biogeochemical Dynamics.* Princeton, NJ: Princeton University Press.

Sathyendranath, S., Jackson, T., Brockmann, C., Brotas, V., Calton, B., Chuprin, A., … Platt, T. (2023). *ESA Ocean Colour Climate Change Initiative (Ocean_Colour_cci): Version 6.0, 4km resolution data.* NERC EDS Centre for Environmental Data Analysis. doi: 10.5285/5011D22AAE5A4671B0CBC7D05C56C4F0

Shutler, J. D., Gruber, N., Findlay, H. S., Land, P. E., Gregor, L., Holding, T., … Gaultier, L. (2024). The increasing importance of satellite observations to assess the ocean carbon sink and ocean acidification. *Earth-Science Reviews*, 104682. doi: 10.1016/j.earscirev.2024.104682

Shutler, J. D., Wanninkhof, R. H., Nightingale, P. D., Woolf, D. K., Bakker, D. C., Watson, A. J., … Donlon, C. J. (2020). Satellites will address critical science priorities for quantifying ocean carbon. *Frontiers in Ecology and the Environment*, *18*(1), 27–35. doi: 10.1002/fee.2129

Song, Z., Yu, S., Bai, Y., Guo, X., He, X., Zhai, W., & Dai, M. (2023). Construction of a High Spatiotemporal Resolution Dataset of Satellite-Derived pCO2 and Air–Sea CO2 Flux in the South China Sea (2003–2019). *IEEE Transactions on Geoscience and Remote Sensing*, *61*, 1–15. doi: 10.1109/TGRS.2023.3306389

Sutton, A. J., Feely, R. A., Maenner-Jones, S., Musielwicz, S., Osborne, J., Dietrich, C., … Weller, R. A. (2019). Autonomous seawater pCO 2 and pH time series from 40 surface buoys and the emergence of anthropogenic trends. *Earth System Science Data*, *11*(1), 421–439. doi: 10.5194/essd-11-421-2019

Sutton, A. J., Sabine, C. L., Maenner-Jones, S., Lawrence-Slavas, N., Meinig, C., Feely, R. A., … Kozyr, A. (2014). A high-frequency atmospheric and seawater pCO2 data set from 14 open-ocean sites using a moored autonomous system. *Earth System Science Data*, *6*(2), 353–366. doi: 10.5194/essd-6-353-2014

Sutton, A. J., Wanninkhof, R. H., Sabine, C. L., Feely, R. A., Cronin, M. F., & Weller, R. A. (2017). Variability and trends in surface seawater p CO $_2$ and CO $_2$ flux in the Pacific Ocean. *Geophysical Research Letters*, *44*(11), 5627–5636. doi: 10.1002/2017GL073814

Sutton, A. J., Williams, N. L., & Tilbrook, B. (2021). Constraining Southern Ocean CO2 Flux Uncertainty Using Uncrewed Surface Vehicle Observations. *Geophysical Research Letters*, *48*(3), 1–9. doi: 10.1029/2020GL091748

Sweeney, C., Gloor, E., Jacobson, A. R., Key, R. M., McKinley, G. A., Sarmiento, J. L., & Wanninkhof, R. H. (2007). Constraining global air-sea gas exchange for CO2 with recent bomb 14C measurements. *Global Biogeochemical Cycles*, *21*(2), 1–10. doi: 10.1029/2006GB002784

Taburet, G., Sanchez-Roman, A., Ballarotta, M., Pujol, M.-I., Legeais, J.-F., Fournier, F., … Dibarboure, G. (2019). DUACS DT2018: 25 years of reprocessed sea level altimetry products. *Ocean Science*, *15*(5), 1207–1224. doi: 10.5194/os-15-1207-2019

Takahashi, T., Sutherland, S. C., Wanninkhof, R. H., Sweeney, C., Feely, R. A., Chipman, D. W., … de Baar, H. J. (2009). Climatological mean and decadal change in surface ocean pCO2, and net sea–air CO2 flux over the global oceans. *Deep Sea Research Part II: Topical Studies in Oceanography*, *56*(8-10), 554–577. doi: 10.1016/j.dsr2.2008.12.009

Tans, P. P., & Keeling, R. F. (2023). *Global Monitoring Laboratory - Carbon Cycle Greenhouse Gases.*

Telszewski, M., Chazottes, A., Schuster, U., Watson, A. J., Moulin, C., Bakker, D. C. E., … Wanninkhof, R. (2009). Estimating the monthly $p\mathrm{CO}_2$ distribution in the North Atlantic using a self-organizing neural network. *Biogeosciences*, *6*(8), 1405–1421. doi: 10.5194/bg-6-1405-2009

Torres, O., Kwiatkowski, L., Sutton, A. J., Dorey, N., & Orr, J. C. (2021). Characterizing Mean and Extreme Diurnal Variability of Ocean CO 2 System Variables Across Marine Environments. *Geophysical Research Letters*, *48*(5), 1–12. doi: 10.1029/2020GL090228

Turi, G., Lachkar, Z., & Gruber, N. (2014). Spatiotemporal variability and drivers of $p\mathrm{CO}_2$ and air–sea CO_2 fluxes in the California Current System: An eddy-resolving modeling study. *Biogeosciences*, *11*(3), 671–690. doi:

10.5194/bg-11-671-2014

Wanninkhof, R., Pickers, P. A., Omar, A. M., Sutton, A., Murata, A., Olsen, A., . . . Schuster, U. (2019). A Surface Ocean CO2 Reference Network, SOCONET and Associated Marine Boundary Layer CO2 Measurements. *Frontiers in Marine Science*, *6*.

Wanninkhof, R. H. (2014). Relationship between wind speed and gas exchange over the ocean revisited. *Limnology and Oceanography: Methods*, *12*(6), 351–362. doi: 10.4319/lom.2014.12.351

Weiss, R. (1974). Carbon dioxide in water and seawater: The solubility of a non-ideal gas. *Marine Chemistry*, *2*(3), 203–215. doi: 10.1016/0304-4203(74)90015-2

Weiss, R., & Price, B. (1980). Nitrous oxide solubility in water and seawater. *Marine Chemistry*, *8*(4), 347–359. doi: 10.1016/0304-4203(80)90024-9

Whitt, D. B., Nicholson, S. A., & Carranza, M. M. (2019). Global Impacts of Subseasonal (<60 Day) Wind Variability on Ocean Surface Stress, Buoyancy Flux, and Mixed Layer Depth. *Journal of Geophysical Research: Oceans*, *124*(12), 8798–8831. doi: 10.1029/2019JC015166

Woolf, D. K., Land, P. E., Shutler, J. D., Goddijn-Murphy, L., & Donlon, C. J. (2016). On the calculation of air-sea fluxes of CO 2 in the presence of temperature and salinity gradients. *Journal of Geophysical Research: Oceans*, *121*(2), 1229–1248. doi: 10.1002/2015JC011427

Ye, H., Morozov, E., Tang, D., Wang, S., Liu, Y., Li, Y., & Tang, S. (2020). Variation of pCO2 concentrations induced by tropical cyclones "wind-Pump" in the middlelatitude surface oceans: A comparative study. *PLoS ONE*, *15*(3). doi: 10.1371/journal.pone.0226189

Yu, P., Wang, Z. A., Churchill, J., Zheng, M., Pan, J., Bai, Y., & Liang, C. (2020). Effects of Typhoons on Surface Seawater pCO2 and Air-Sea CO2 Fluxes in the Northern South China Sea. *Journal of Geophysical Research: Oceans*, *125*(8). doi: 10.1029/2020JC016258

Acknowledgments

We are indebted to the large number of scientists who have measured the surface ocean $f\mathrm{CO_2}$ over the last few decades, and to the programs and agencies that enabled or funded these observations. We are also very grateful to all those who have assembled and quality controlled these observations into readily usable products. A special thanks to the Surface Ocean CO2 Atlas (SOCAT) team under leadership of Dorothee Bakker. SOCAT is an international effort, endorsed by the International Ocean Carbon Coordination Project (IOCCP), the Surface Ocean Lower Atmosphere Study (SOLAS) and the Integrated Marine Biosphere Research (IMBeR) program, to deliver a uniformly quality-controlled surface ocean CO2 database. We are also grateful to the many other programs that have collected and processed marine observations in the last few decades, enabling the development of novel statistical techniques for interpreting the CO_2 observations. The work of LG, JS, and NG was supported by the ESA OceanHealth-OA project (contract number 4000137603/22/I-DT). JS has received further support by the ESA MAXSS project (4000132954/20/I-NB). The Ssalto/Duacs altimeter products were produced and distributed by the Copernicus Marine and Environment Monitoring Service (CMEMS) (http://www.marine.copernicus.eu).